

Localized Myosin II Activity Regulates Assembly and Plasticity of the Axon Initial Segment

Highlights

- Phosphorylated myosin light chain (pMLC) is enriched in axon initial segments (AISs)
- pMLC is associated with the actin rings in the AIS, as imaged by STORM
- Inhibiting MLC phosphorylation and myosin II activity blocks assembly of the AIS
- pMLC is rapidly lost with depolarization, destabilizing actin and the AIS

Authors

Stephen L. Berger,
Alejandra Leo-Macias,
Stephanie Yuen, ..., Mario Delmar,
Christophe Leterrier, James L. Salzer

Correspondence

james.salzer@nyumc.org

In Brief

Berger et al. demonstrate that pMLC, a key regulator of contractile myosin II, is enriched in the axon initial segment (AIS) and is associated with actin rings. They show that pMLC and myosin II have major roles in AIS assembly and activity-dependent plasticity.



Localized Myosin II Activity Regulates Assembly and Plasticity of the Axon Initial Segment

Stephen L. Berger,¹ Alejandra Leo-Macias,² Stephanie Yuen,¹ Latika Khatri,¹ Sylvia Pfennig,¹ Yanqing Zhang,¹ Esperanza Agullo-Pascual,² Ghislaine Caillol,³ Min-Sheng Zhu,⁴ Eli Rothenberg,⁵ Carmen V. Melendez-Vasquez,^{6,7} Mario Delmar,² Christophe Leterrier,³ and James L. Salzer^{1,8,*}

¹Neuroscience Institute and Department of Neuroscience and Physiology, NYU School of Medicine, New York, NY 10016, USA

²Division of Cardiology, NYU School of Medicine, New York, NY 10016, USA

³Aix Marseille Université, CNRS, INP UMR7051, 13344 Cedex 15, Marseille, France

⁴Model Animal Research Center and MOE Key Laboratory of Model Animal and Disease Study, Nanjing University, Nanjing 210061, China

⁵Department of Biochemistry and Molecular Pharmacology, NYU School of Medicine, New York, NY 10016, USA

⁶Department of Biological Sciences, Hunter College, New York, NY 10065, USA

⁷Department of Molecular, Cellular, and Developmental Biology, The Graduate Center, The City University of New York, NY 10016, USA

⁸Lead Contact

*Correspondence: james.salzer@nyumc.org

<https://doi.org/10.1016/j.neuron.2017.12.039>

SUMMARY

The axon initial segment (AIS) is the site of action potential generation and a locus of activity-dependent homeostatic plasticity. A multimeric complex of sodium channels, linked via a cytoskeletal scaffold of ankyrin G and beta IV spectrin to submembranous actin rings, mediates these functions. The mechanisms that specify the AIS complex to the proximal axon and underlie its plasticity remain poorly understood. Here we show phosphorylated myosin light chain (pMLC), an activator of contractile myosin II, is highly enriched in the assembling and mature AIS, where it associates with actin rings. MLC phosphorylation and myosin II contractile activity are required for AIS assembly, and they regulate the distribution of AIS components along the axon. pMLC is rapidly lost during depolarization, destabilizing actin and thereby providing a mechanism for activity-dependent structural plasticity of the AIS. Together, these results identify pMLC/myosin II activity as a common link between AIS assembly and plasticity.

INTRODUCTION

The axon initial segment (AIS) has multiple critical roles in the organization and function of neurons. It is the site of action potential generation (Bender and Trussell, 2012; Kole and Stuart, 2012), reflecting the striking enrichment of voltage-gated sodium channels (NaV) at this site. The AIS is also a locus of homeostatic plasticity, resulting from activity-dependent remodeling of the abundance and distribution of NaV and other AIS components over several timescales (Yamada and Kuba, 2016). In addition, the AIS has an essential role in neuronal polarity by providing a barrier to the ingress of somatodendritic components into the

axon (Hedstrom et al., 2008; Sobotzik et al., 2009). Finally, the AIS receives synaptic input from chandelier cells, a specialized type of interneuron, allowing for coordinate regulation of the activity of cortical projection neurons (Wang et al., 2016).

These various AIS functions depend on the local enrichment of a macromolecular complex comprised of voltage-gated ion channels, the cell adhesion molecules (CAMs) neurofascin 186 (NF186) and NrCAM, and a specialized submembranous scaffold of ankyrin G (AnkG) and beta-IV (β IV) spectrin. NaV, the CAMs, and the voltage-gated potassium channels KCNQ2 and KCNQ3 all bind to AnkG, which itself binds near the C terminus of β IV spectrin (Bennett and Lorenzo, 2016; Zhang and Rasband, 2016). Indeed, AnkG is essential for AIS assembly and its long-term stability (Hedstrom et al., 2008; Sobotzik et al., 2009). AnkG also promotes the assembly of a similar electrogenic complex of NaV, NF186, and β IV spectrin at CNS and peripheral nervous system (PNS) nodes of Ranvier (Dzhashiashvili et al., 2007), sites of action potential regeneration in myelinated axons.

A key question is how this complex is assembled and directed to the proximal region of axons. The AIS is intrinsically specified, assembling via an inside-out mechanism by first organizing its cytoskeleton and subsequently recruiting channels and adhesion molecules to this scaffold (Dzhashiashvili et al., 2007; Jenkins and Bennett, 2001). Recent super-resolution microscopy studies indicate that the AIS complex is tethered to a series of submembranous, circumferential actin rings (Xu et al., 2013). These rings are regularly arrayed along the AIS at \sim 190 nm intervals, spacing likely dictated by spectrin tetramers that bridge the actin rings (Leterrier et al., 2015; Zhong et al., 2014). Accordingly, β IV spectrin, AnkG, and NaV are organized with a corresponding repeat structure in the AIS (Xu et al., 2013). While these actin rings likely coordinate the micro-architecture within the AIS, they are not sufficient to restrict the AIS complex to the proximal axon, as actin rings are present throughout the entire axon. Distal to the AIS, actin rings are organized by β II spectrin, which, in turn, tethers ankyrin B (Davis et al., 2009; Xu et al., 2013; Zhong et al., 2014). Rings have also been visualized in dendrites and glial processes (D'Este et al., 2016; He et al., 2016).



Thus, other mechanisms must contribute to the enrichment of AnkG and β IV spectrin in the proximal axon. One proposed mechanism is competition between the proximal AnkG and distal ankyrin B (AnkB) axonal cytoskeletons during development, which regulates AIS length; this competition enhances (Galiano et al., 2012), but is not essential (Lorenzo et al., 2014), for AnkG targeting to the proximal axon. The microtubule cytoskeleton also promotes localization of AnkG to the proximal axon via direct interactions with the microtubule end-binding proteins EB1 and EB2 (Fréal et al., 2016) and as a result of local acetylation of microtubules in the AIS (Tapia et al., 2010).

An alternative and complementary possibility is that the actin cytoskeleton in the proximal axon is itself modified in a manner that promotes recruitment and/or stability of the AnkG/ β IV spectrin cytoskeleton. A potential candidate to modify actin is myosin II, the classical actin-directed motor protein. Distinct non-muscle myosin IIs are expressed in all vertebrate cells (Sellers, 2000; Vicente-Manzanares et al., 2009). Myosin II forms a hexameric structure comprised of two actin-binding myosin heavy chains (MHCs), two essential light chains (ELCs), and two regulatory myosin light chains (MLCs). Like smooth muscle myosin, non-muscle myosin II is activated via MLC phosphorylation, either by an initial mono- (Ser19) or by sequential diphosphorylation (Thr18/Ser19) (Heissler and Sellers, 2014). MLC phosphorylation activates both the contractile actin-directed ATPase function of non-muscle myosin II and the assembly of multimeric myosin filaments required for coordinate force generation (Vicente-Manzanares et al., 2009). These contractile functions of myosin II play a key role in a variety of motile cellular structures, including neurite growth cones (Brown and Bridgman, 2003), and in the organization and tensioning of non-motile structures, including cell contact sites (Salomon et al., 2017) such as adherens junctions (Ma and Adelstein, 2014).

Here we show that diphosphorylated myosin light chain (pMLC) is strikingly enriched in the AIS, where it associates with actin rings based on super-resolution fluorescence microscopy. pMLC accumulates concurrently with AIS assembly, regulated by a balance of kinase and phosphatase activities. Both pMLC and myosin II activity are essential for AIS assembly and the fidelity of its distribution. During depolarization, pMLC is rapidly lost, enabling activity-dependent plasticity of the AIS via actin destabilization. These results implicate pMLC and contractile myosin II in delineating the actin cytoskeleton of the proximal axon and as common mechanistic links between AIS assembly and plasticity.

RESULTS

pMLC Demarcates Electrogenic Domains of Axons

Using a well-characterized antibody specific to diphosphorylated non-muscle MLC (Hirano and Hirano, 2016; Salomon et al., 2017), we found pMLC is substantially enriched in the AIS of mature 10 days in vitro (DIV10) cultured hippocampal (Hc) neurons (Figure 1A). pMLC co-localized with AnkG in the AIS (Figure 1A), but not with Kv2.1 (Figure S1A), which is present in an ankyrin-independent subdomain of the AIS (King et al., 2014). pMLC was also detected in the nucleus and in discrete perinuclear structures resembling the Golgi apparatus and vesi-

cles. It was essentially absent from the axon distal to the AIS and in dendrites. pMLC staining in Hc neurons was abolished by pre-treatment with calf intestinal phosphatase (CIP) (Figure S1B) or lambda phosphatase (data not shown), as was the single ~20-kDa pMLC band detected by western blots when Hc neuron lysates were pre-treated with CIP or lambda phosphatase (Figure S1C), underscoring the specificity of the antibody.

Consistent with the staining of cultured neurons, there was uniform enrichment of pMLC in the AIS of neurons in the adult mouse brain, including the cortex (Figure 1B), hippocampus, striatum, and cerebellum (data not shown). pMLC was similarly enriched at CNS and PNS nodes of Ranvier, as evident in rat optic nerves (Figure 1C) and sciatic nerves (Figure 1D), respectively. pMLC was also consistently present in heminodes and mature nodes in myelinating cocultures of dorsal root ganglia and Schwann cells (Figure S1D). Confocal imaging of sciatic nerves demonstrated that pMLC has a circumferential localization at nodes (Figure S1E) akin to other components of the NaV/AnkG cytoskeletal complex.

The accumulation of pMLC in the AIS is due to a local increase in MLC phosphorylation rather than enrichment of MLC or myosin II at this site. Thus, total MLC and other components of the myosin II hexamer, i.e., ELC (*Myf6*) and two of the non-muscle myosin II heavy chains, MHCII-B and -C (*Myh10* and *Myh14*, respectively), were widely expressed in all compartments of mature cultured neurons (Figure S2A). MHCII-A (*Myh9*) expression was more restricted to the nucleus (Figure S2A). The three mammalian MLC isoforms (*Myf9*, *Myf12a*, and *Myf12b*) cannot be distinguished by available antibodies due to their close sequence homology (Park et al., 2011). Virally mediated expression of individual GFP-tagged MLC isoforms in Hc neurons similarly revealed that they are broadly distributed (data not shown). Based on qPCR, *Myf12b* was the predominant isoform present in cultured Hc neurons and throughout the adult rat nervous system (Figure S2B).

pMLC Is an Early and Integral Component of the AIS

To assess a potential role of pMLC in the AIS assembly, we compared the temporal accumulation of pMLC versus AnkG. Cultured Hc neurons were fixed and stained at daily intervals between DIV2 and DIV6. At DIV2, corresponding to stage 3, the axon is specified but the AIS is not yet demarcated (Dotti et al., 1988). At this early time point, there was a modest enrichment of pMLC along the entire length of the nascent axon, identified as the longest neurite (Figure 2A), suggesting pMLC is an early axonal component. pMLC is also present in the growth cone at this and later stages in agreement with a described role of myosin II at this site (Brown and Bridgman, 2004). pMLC was enriched in the earliest initial segments as visualized by AnkG, beginning at DIV3. Thereafter, pMLC and AnkG co-accumulated in the AIS with essentially identical time courses and spatial distributions (Figures 2B and 2C). In parallel, both pMLC and AnkG levels progressively decreased in the axon distal to the AIS, reaching background levels by DIV10 (Figure 2D). pMLC levels decreased 3.8-fold ($p < 0.0001$) and AnkG levels decreased 3.8-fold ($p < 0.0001$) in the axon distal to the AIS at DIV10 compared to DIV4. Together, these results implicate pMLC as an early marker of the axon and, with AnkG, an early component

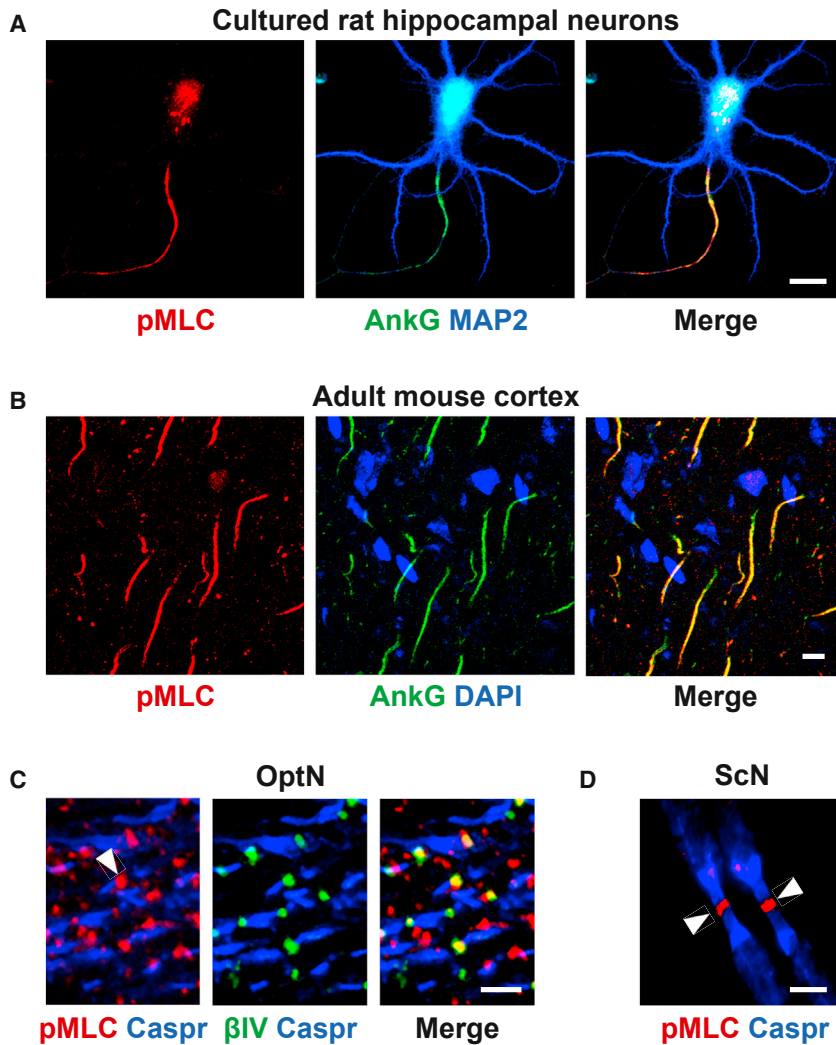


Figure 1. Phosphorylated Myosin Light Chain Is Enriched at the AIS and Nodes of Ranvier

(A) DIV10 cultured rat hippocampal neuron showing colocalization of pMLC (red) with Ankg (green) in the AIS. Soma and dendrites are counterstained with MAP2 (blue). Scale bar, 10 μ m.

(B) Post-natal day (P)30 mouse cortex showing colocalization of pMLC (red) and Ankg (green) in the AIS of projection neurons. Nuclei are stained with Hoechst (blue). Scale bar, 5 μ m.

(C) Adult rat optic nerve (OptN) sections show pMLC (red) is enriched at nodes of Ranvier stained with β IV spectrin (green) and flanked by the paranodal marker Caspr (blue). White arrowhead labels an example node. pMLC is also present in some non-nodal structures. Scale bar, 5 μ m.

(D) Teased adult rat sciatic nerve (ScN) fibers show localization of pMLC (red) at nodes of Ranvier, flanked by the paranodal marker Caspr (blue). White arrowheads label nodes. Scale bar, 5 μ m.

See also Figures S1 and S2.

Phosphorylation of MLC and Myosin II Activity Are Required for AIS Assembly

The early accumulation of pMLC in the AIS suggested that local contractile myosin II activity contributes to AIS assembly. To test this possibility directly, we treated cultures with blebbistatin, an inhibitor widely used to block the actin-directed ATPase activity of non-muscle myosin II in cells (Kovács et al., 2004; Straight et al., 2003). Treatment of Hc neuron cultures with 20 μ M blebbistatin from DIV3 to DIV6 resulted in a striking reduction (62%, $p < 0.0001$) in the accumulation of Ankg (Figures 3A–3C) and NF186 (data not

shown) in the AIS, compared to vehicle-treated Hc neuron cultures. These results provide compelling evidence that myosin II contractility has an essential role in the assembly of the AIS. Interestingly, pMLC was much less affected (35% decrease, $p = 0.0001$), consistent with reports that blebbistatin affects the ATPase activity and contractility of the MHCs, not the phosphorylation of MLC (Kovács et al., 2004; Straight et al., 2003). In agreement with prior reports (Flynn et al., 2009; Kollins et al., 2009), blebbistatin treatment also increased the branching and length of axons (Figure S3F); no effect on dendrite morphology was evident by visual inspection.

We next addressed the role of MLC phosphorylation in AIS assembly. We treated Hc neurons at DIV4, during peak AIS assembly, with a series of pharmacological inhibitors to known MLC kinases (Table S1), including MLC kinase (MLCK) and Rho-associated kinase (ROCK) (Heissler and Sellers, 2014; Newell-Litwa et al., 2015). Of these, only treatment with ML7, a well-characterized MLCK inhibitor (Saitoh et al., 1987), significantly reduced pMLC levels at the AIS (Figures 3D–3F). ROCK inhibition with Y27632 (Uehata et al., 1997) had no effect on pMLC levels in the AIS, although it did significantly reduce pMLC levels

of the AIS. They also indicate that the proximal increase of pMLC and Ankg is accompanied by their active reduction in the axon distal to the AIS.

We next assessed whether pMLC is incorporated into the cytoskeletal scaffold at the AIS. Similar to other cytoskeletal components, e.g., Ankg and β IV spectrin (Zhang et al., 2012), pMLC was not extracted by treatment of live DIV10 Hc neurons with the detergent Triton X-100 (Figure S3A). To examine whether pMLC accumulation depends on other AIS components, we performed a small hairpin RNA (shRNA) knockdown of Ankg, which is known to block AIS assembly (Hedstrom et al., 2008). Ankg knockdown effectively prevented pMLC accumulation in the proximal axon (Figures S3B and S3C). Thus, 84% of the proximal axons in control-infected neurons were pMLC+, whereas only 5.6% of Ankg knockdown neurons were pMLC+. The shRNA knockdowns of β IV spectrin and NaV yielded similar results, with proportionate reductions of these AIS components and pMLC (Figures S3D and S3E). Together, these results indicate pMLC is an integral component of the AIS and that its recruitment and/or stability requires Ankg.

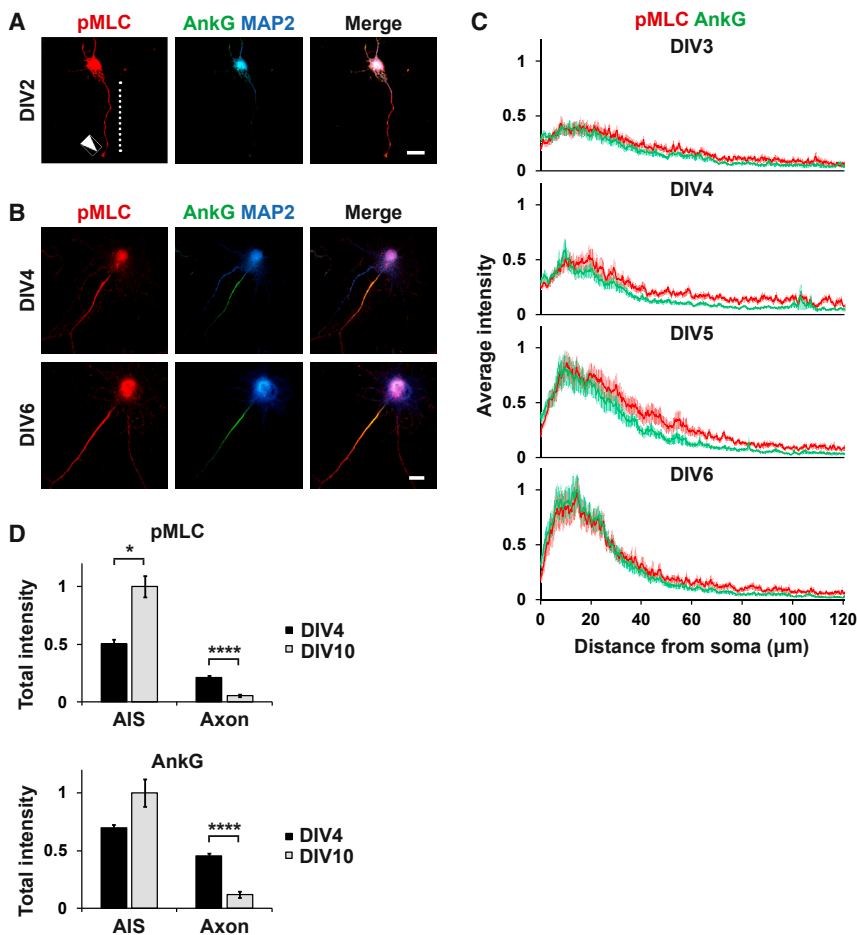


Figure 2. pMLC Accumulation in Axons and the AIS during Development

(A) At DIV2, pMLC (red) is present throughout the neuron with moderate enrichment in the nascent axon (dotted white line) and growth cone (arrowhead). There is minimal expression of AnkG (green) and MAP2 (blue) in the axon at this stage. Scale bar, 10 μ m.

(B) pMLC (red) is enriched in the developing AIS, where it colocalizes with AnkG (green) at DIV4 and DIV6; pMLC is present at reduced levels in the axon as well. MAP2 (blue) labels the somatodendritic compartment. Scale bar, 10 μ m.

(C) Spatial intensity profiles of pMLC (red) and AnkG (green) demonstrate gradual proximal enrichment between DIV3 and DIV6. Intensities are normalized in each case to their corresponding DIV6 peaks. Graphs show average intensities \pm SEM.

(D) pMLC and AnkG increase in the AIS and decrease in the axon during maturation. Average AIS intensity \pm SEM is compared between DIV4 (black) and DIV10 (gray). Kruskal-Wallis test with Dunn's correction, * $p < 0.05$, ** $p < 0.01$, and **** $p < 0.0001$.

in stress fibers of the occasional contaminating astrocyte in the same cultures (data not shown). These results implicate MLCK as the primary MLCK in the AIS during development.

Of note, the inhibition of MLCK with ML7 in DIV4 Hc neurons also reduced AnkG levels in the AIS (Figures 3D–3F), implicating MLCK and, thus, pMLC levels as important determinants of AIS assembly. Peak pMLC and AnkG levels decreased \sim 60% and \sim 50%, respectively (Figure 3E), and over the entire AIS, levels decreased by 41% ($p = 0.0001$) and 31% ($p = 0.0066$), respectively (Figure 3F). In contrast, acute treatment of DIV10 Hc neurons with blebbistatin (Figure S3G), the MLCK inhibitor ML7 (Figure S3H), and various other kinase inhibitors (Figure S3H; Table S1) had no evident effect on pMLC levels or the AIS. Thus, the mature AIS is resistant to inhibitor treatment compared to the developing AIS, likely reflecting its stability after formation.

Inhibition of Myosin Phosphatase Results in Ectopic AIS Expression in the Axon

We next assessed the effects of increasing phosphorylation of MLC on the expression and distribution of AIS components in the proximal and distal axon. The serine/threonine phosphatase PP1c β/δ , which has a large number of substrates, dephosphorylates MLC when it is bound to either MYPT1 or MYPT2, two well-known myosin-targeting subunits (Grassie et al., 2011). Based on PCR, both subunits were expressed in rodent

Hc neurons, along with three additional, less well-characterized MYPT homologs (Figure S4A). Therefore, to assess the role of myosin phosphatase, we used pharmacological inhibitors to PP1 as well as genetic strategies to downregulate MYPT1 and MYPT2 expression.

We first confirmed that PP1 is the relevant catalytic phosphatase using pharma-

cological inhibitors to several serine/threonine phosphatases. We treated DIV10 neurons with calyculin A, a well-characterized pan-PP1 and PP2A inhibitor (Kato et al., 1988), for just 30 min to limit toxicity. Calyculin treatment significantly increased pMLC, but not total MLC levels, in neurons based on blots (Figures S4B and S4C) and on staining of both the AIS (1.46-fold increase, $p = 0.0332$) and remainder of the axon (4-fold increase, $p < 0.0001$) (Figures S4D–S4H). This brief calyculin treatment did not increase AnkG in the AIS, but it did result in a small but significant increase of AnkG in the distal axon (Figure S4H; 67% increase, $p = 0.0002$). A similar effect on pMLC levels in the AIS was seen with okadaic acid, which is a dual PP1/PP2A inhibitor when used at high concentrations (1 μ M) (data not shown). In contrast, inhibiting other phosphatases, i.e., PP2A with fostriecin and low concentrations of okadaic acid (2 nM), or calcineurin (PP3) with cyclosporin A (CsA) and FK506, reduced pMLC levels in the AIS by 38% (fostriecin, $p = 0.1805$) and 50% (CsA, $p = 0.0023$), respectively (Figure S4E). The reductions of pMLC levels by fostriecin and CsA presumably resulted from indirect effects on myosin kinases or phosphatases. Together, these results implicate PP1 rather than PP2A or calcineurin in the dephosphorylation of pMLC in the AIS.

To assess the role of the PP1c-targeting myosin phosphatase subunits, we knocked out MYPT1 and knocked down MYPT2 in cultured mouse Hc neurons. Wild-type mouse neurons

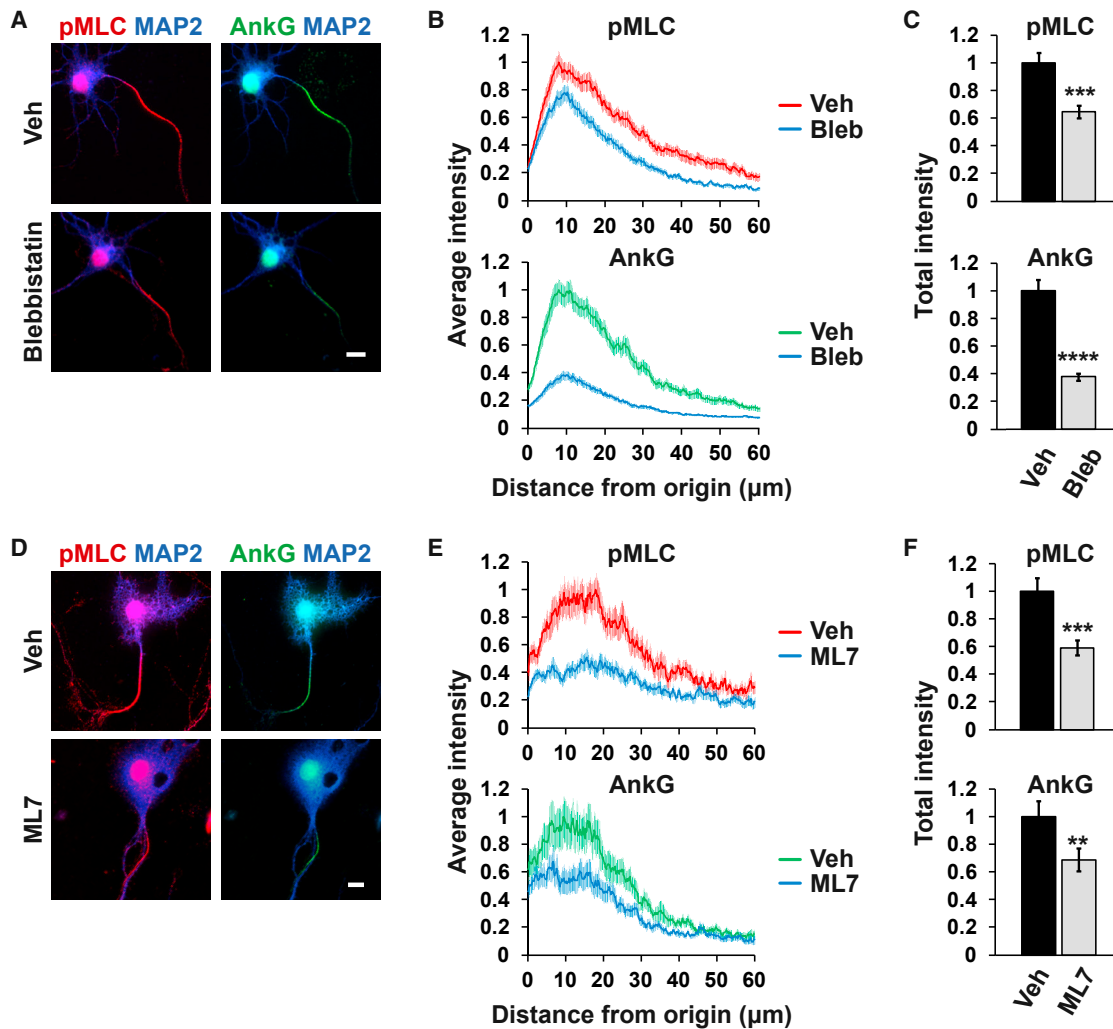


Figure 3. Myosin II Activity and Phosphorylation of MLC Are Required for AIS Assembly

(A) Treatment with the myosin ATPase inhibitor blebbistatin reduces AnkG intensity at the developing AIS. Cultures were treated from DIV3 to DIV6. MAP2 (blue) is also shown. Scale bar, 20 μ m.

(B) Spatial intensity profiles of DIV6 axons demonstrate slightly reduced pMLC (red) and substantially reduced AnkG (green) levels after blebbistatin treatment (blue).

(C) Average intensities \pm SEM of pMLC and AnkG after treatment with vehicle (black) or blebbistatin (gray). Mann-Whitney test, *** $p \leq 0.001$ and **** $p < 0.0001$.

(D) A 3-hr incubation with the MLCK inhibitor ML7 decreased pMLC (red) and AnkG (green) levels compared to vehicle (veh) controls in DIV4 neurons. MAP2 (blue) is also shown. Scale bar, 10 μ m.

(E) Spatial intensity profiles of DIV4 axons show reduced pMLC (red) and AnkG (green) intensities after ML7 treatment (blue). Graphs show average intensities \pm SEM and are normalized to the control peak.

(F) Average intensities \pm SEM of pMLC and AnkG after treatment with vehicle (black) or ML7 (gray). Mann-Whitney test, ** $p \leq 0.01$ and *** $p \leq 0.001$.

See also Figure S3.

assemble an AIS in culture with a time course similar to that of rat Hc neurons, although with a less uniform and stereotypic appearance. To knock out MYPT1, we infected cultured mouse Hc neurons isolated from *MYPT1^{fl/fl}* mice (He et al., 2013) with an adeno-associated virus (AAV)1 encoding Cre or, as a control, EGFP. To knock down MYPT2, we infected mouse Hc neurons with a lentivirus encoding a shRNA to MYPT2 (shMYPT2) or, as a control, a scrambled sequence (shScr). In both cases, neurons were infected on DIV1, and the AIS and axons were analyzed on DIV12 to ensure sufficient time for loss of the

corresponding protein. Axons in both the MYPT1 knockout and MYPT2 knockdown neurons appeared normal based on visual inspection; levels of the axonal marker Tau were also unchanged (data not shown).

Loss of either MYPT1 or MYPT2 increased pMLC levels in the AIS and elsewhere along the axon similar to acute calyculin treatment, but without evident cytotoxicity. With the longer time course of MYPT depletion, there was also an effect on the distribution of AnkG. In the MYPT1 knockout neurons (Figures 4A–4D), pMLC levels were roughly double in the AIS

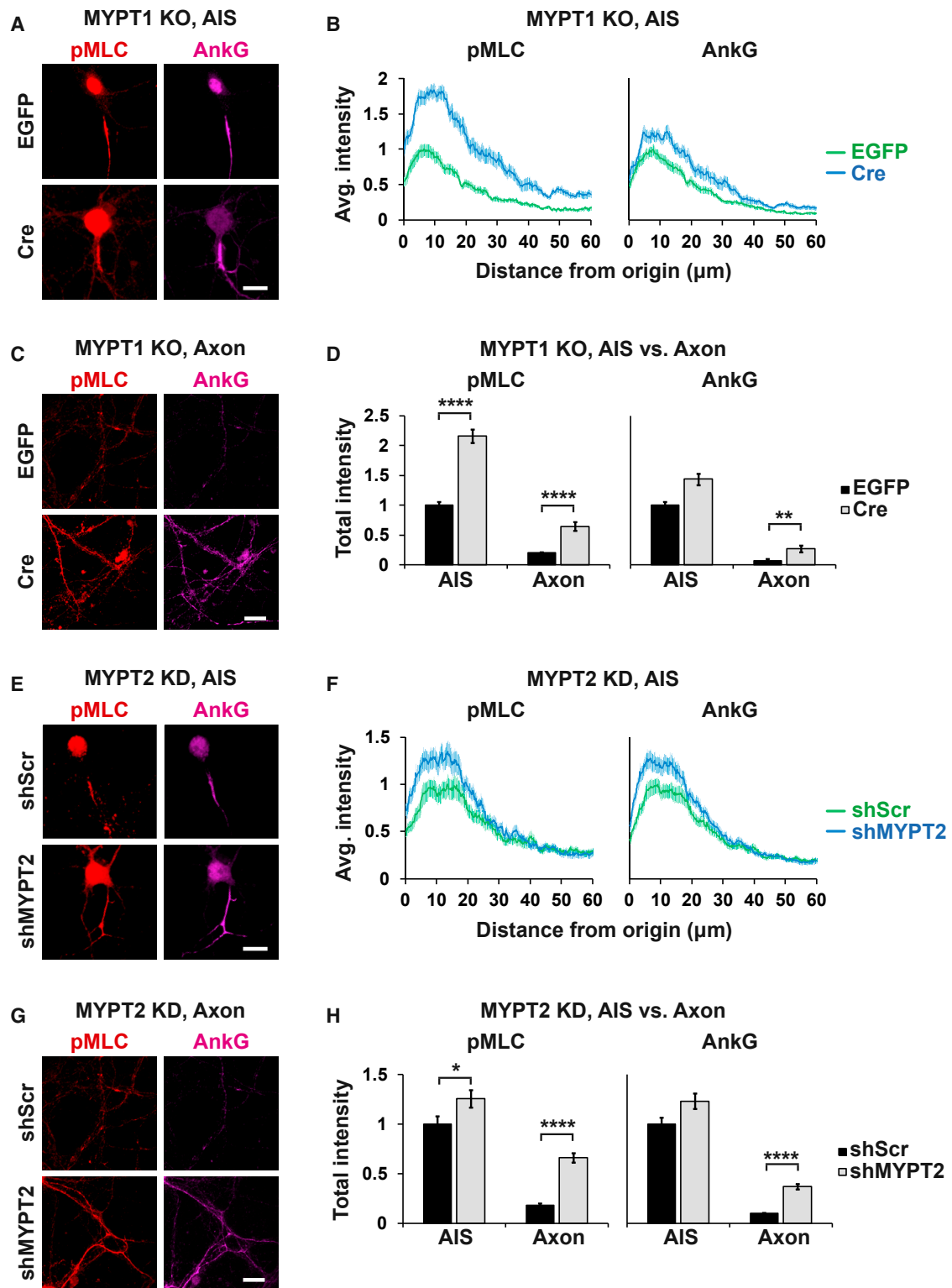


Figure 4. Loss of MYPT Subunits Increases pMLC and Ectopic Expression of AIS Proteins

(A) Mouse neurons were infected with AAV1-EGFP (control; top panels) or AAV1-Cre (knockout; bottom panels) on DIV1 and fixed on DIV12. MYPT1 knockout enhances pMLC (red) and AnkG (magenta) at the AIS. Scale bar, 20 μm .

(B) Spatial intensity profiles demonstrate elevated pMLC and AnkG levels in MYPT1 knockout (KO, blue) versus control (green) neurons. Graphs show average intensities \pm SEM normalized to the control peak.

(legend continued on next page)

(116% increase versus control, $p < 0.0001$), whereas AnkG levels were modestly increased (44% increase, $p = 0.0939$) (Figure 4D). Of note, both pMLC and AnkG were significantly increased at sites in the axon distal to and not contiguous with the AIS (pMLC, 3.2-fold increase, $p < 0.0001$; AnkG, 4.1-fold increase, $p = 0.0017$) (Figures 4C and 4D). The levels of pMLC and AnkG in these knockout axons represented substantial increases over basal levels, approaching $\sim 65\%$ and $\sim 27\%$ of control AIS intensity, respectively. In these axonal outposts of increased pMLC and AnkG, staining of both proteins completely overlapped and was associated with corresponding increases in the expression of NaV, β IV spectrin, and NF186 (data not shown).

Loss of MYPT2 produced a similar effect on the distribution of pMLC and AnkG in the AIS and axon (Figures 4E–4H), with a more pronounced effect in the axon distal to the AIS. In the AIS, there were modest increases of both pMLC (26% increase, $p = 0.0489$) and AnkG (23% increase, $p = 0.0517$). Both pMLC and AnkG were significantly increased in the axon distal to the AIS (3.6-fold increase, $p < 0.0001$ and 3.7-fold increase, $p < 0.0001$, respectively; Figures 4G and 4H). pMLC and AnkG were again frequently present in discrete outposts of staining that reached $\sim 67\%$ and 37% of control AIS intensity, respectively. Combined MYPT1 knockout/MYPT2 knockdown neurons could not be assessed due to significant toxicity by DIV7. These latter results indicate that MYPT1 and MYPT2 have compensating activities required for neuronal viability.

Taken together, these results suggest that elevated pMLC levels, via aberrant activation of myosin II, are sufficient to drive ectopic localization of AIS components in the distal axon.

pMLC Is Rapidly Lost during Depolarization via Ca^{2+} -Dependent Mechanisms

Given its key role in AIS assembly, we examined whether pMLC may contribute to activity-dependent changes in the organization of the AIS. Elevation of extracellular KCl in cultures of Hc neurons is a widely used model of sustained depolarization (Greer and Greenberg, 2008) that has been used to model AIS plasticity (Evans et al., 2015). In time course studies, we found that loss of AIS components following KCl-induced depolarization was much faster than previously reported (Evans et al., 2015). Thus, treatment of rat Hc neurons with 15 or 50 mM KCl resulted in $\sim 40\%$ loss of AnkG and NaV intensity from the AIS after just 60 min of depolarization (Figures S5A–S5C). Similar results were also seen after the depolarization of rat cortical neurons (data not shown), and they were even more pronounced in mouse Hc neurons (see below). AnkG and NaV were lost

throughout the AIS (Figure S5B), and all MAP2+ neurons in the rat hippocampal cultures were affected (Figure S5C). Similar reductions of β IV spectrin and NF186 were also seen, indicating activity disassembles the entire AIS complex (data not shown).

Depolarization of rat Hc neurons resulted in a more striking and rapid loss of pMLC relative to all other AIS components. pMLC levels were substantially reduced after 5 min of depolarization (61% reduction, $p < 0.0001$) and largely gone at 15 and 30 min (83% reduction, $p < 0.0001$) (Figures 5A and 5B). In contrast, reduction of AnkG only became significant at ~ 30 min (35% decrease, $p = 0.004$); reduction of NaV expression likewise required 30–60 min of depolarization (data not shown). pMLC was lost across the entire AIS (Figure 5C), was observed in all MAP2+ neurons, and was more complete than the loss of AnkG in the corresponding neurons (Figure 5D).

As a complement to KCl-evoked depolarization, we examined whether pMLC is also lost from the AIS during patterned optogenetically driven depolarization. We expressed channelrhodopsin II (Zhang et al., 2006) in cultured Hc neurons via an AAV construct. Neurons were infected on DIV2, and they were analyzed at DIV10 when expression was essentially uniform in all neurons based on the Venus reporter. Neurons were stimulated for 15 min with a light-emitting diode (LED, blue diode) using a repetitive burst-like stimulation protocol previously reported to shorten the AIS of cultured neurons after 3 hr (Evans et al., 2015); infected companion cultures that were not photostimulated served as controls. Optogenetic stimulation for only 15 min at 37°C resulted in surprisingly significant losses of pMLC (67% reduction, $p < 0.0001$) and AnkG (49% reduction, $p < 0.0001$) from the AIS (Figures 5E and 5F).

Taken together, these results indicate pMLC is lost early and preferentially from the AIS as the result of sustained activity. A key question is how depolarization results in the loss of pMLC. Surprisingly, despite the decrease in pMLC levels, total MLC protein levels did not change in the proximal axon even after 30 min or more of KCl treatment, based on staining (Figure 5G) and western blotting (Figure 5H). Thus, pMLC, but not total MLC, is specifically and rapidly lost with depolarization. These effects on the AIS were reversible starting at ~ 1 –2 hr after KCl removal, with recovery complete by 3 hr afterward (Figure 5I).

We next examined whether this loss of pMLC resulted from dephosphorylation by PP1c, as suggested by its reversibility and the stable levels of total MLC. Treatment with calyculin (Figure 6A), which elevates baseline pMLC levels in the AIS, resulted in a significant although small increase in the levels of pMLC in the AIS following depolarization (52% increase, $p = 0.0216$); calyculin

(C) Axons distal to the AIS display significant ectopic accumulation of pMLC (red) and AnkG (magenta) after knockout of MYPT1. Scale bar, 20 μm .

(D) Quantification of pMLC and AnkG in the AIS and axon in control (black) or MYPT1 KO (gray) neurons. Graphs are average intensities \pm SEM. Kruskal-Wallis test with Dunn's correction, $**p \leq 0.01$ and $****p < 0.0001$.

(E) MYPT2 knockdown (KD) modestly increases pMLC (red) or AnkG (magenta) at the AIS. Neurons were infected with scrambled (shScr; top panels) or knockdown (shMYPT2; bottom panels) lentivirus on DIV1 and fixed on DIV12. Scale bar, 20 μm .

(F) Spatial intensity profiles demonstrate slight elevation of pMLC and AnkG in MYPT2 knockdown- (blue) versus control- (green) infected AIS. Graphs show average intensities \pm SEM and are normalized to the control peak.

(G) Axons distal to the AIS display substantial accumulation of pMLC (red) and AnkG (magenta) after MYPT2 KD. Scale bar, 20 μm .

(H) Quantification of pMLC and AnkG in the AIS and axon in control (black) or MYPT2 knockdown (gray) neurons. Graphs are average intensities \pm SEM. Kruskal-Wallis test with Dunn's correction, $****p < 0.0001$.

See also Figure S4.

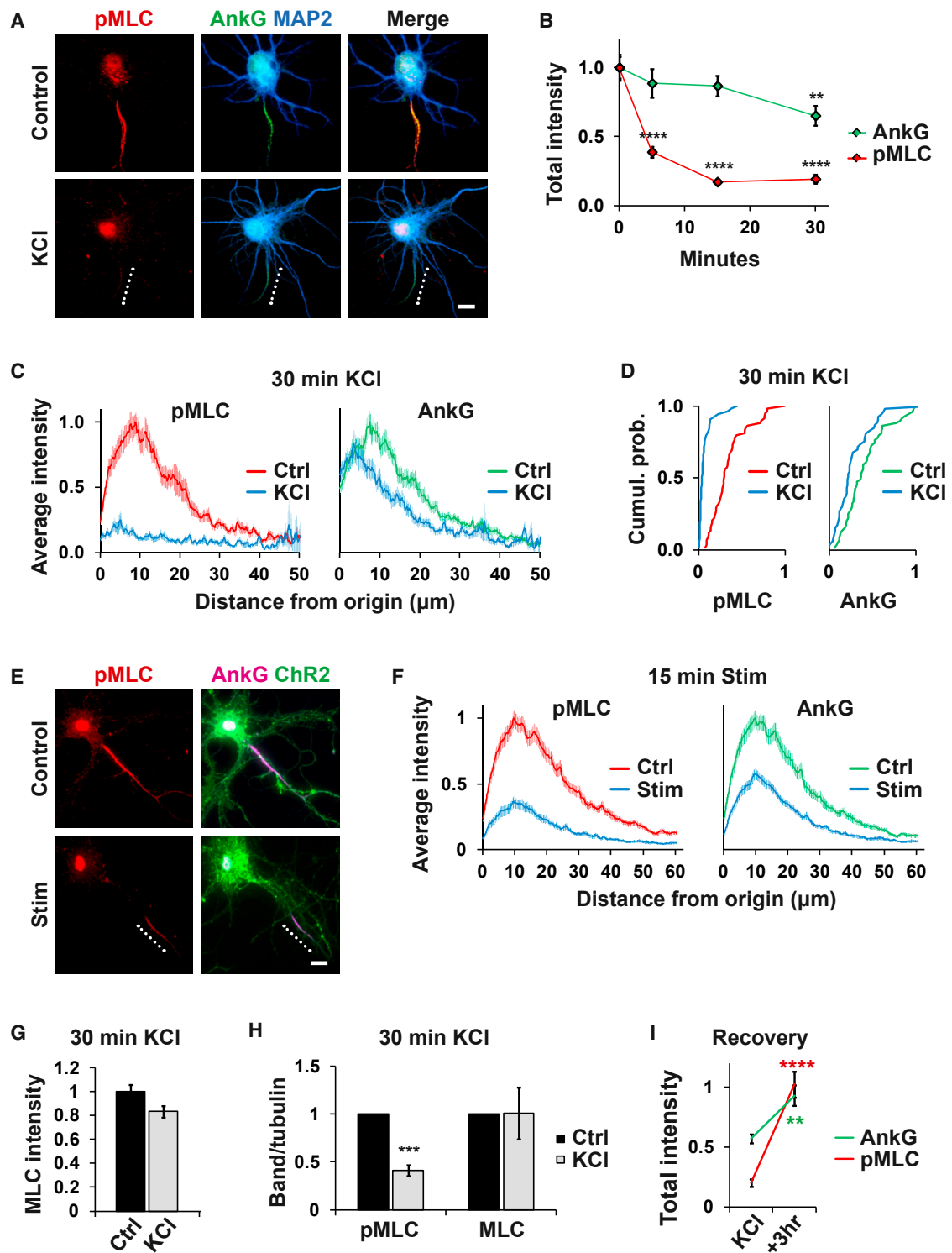


Figure 5. Depolarization Results in Rapid Loss of pMLC in the AIS

(A) Staining for pMLC (red), AnkG (green), and MAP2 (blue) of control (5 mM KCl; top panels) or depolarized (50 mM KCl for 30 min; bottom panels) DIV10 rat Hc neurons. The dotted line demarcates the partially disassembled AIS. Scale bar, 10 μm .

(B) Changes in the AIS staining intensities of pMLC (red) versus AnkG (green) during 30 min of depolarization with 50 mM KCl are shown. Data points are average \pm SEM taken at 0, 5, 15, and 30 min and are normalized to initial intensity. Kruskal-Wallis test with Dunn's correction, ** $p \leq 0.01$ and **** $p < 0.0001$.

(legend continued on next page)

did not affect AnkG levels. Similarly, MYPT1 knockout and MYPT2 knockdown did not prevent AnkG and pMLC loss with depolarization (Figures S6A and S6B). Interestingly, depolarization increased the levels of pMLC, and other AIS components, in the distal axon in wild-type neurons, consistent with an activity-dependent effect on MLC phosphorylation. These increases were further accentuated in the distal axons of the MYPT1 knockout and MYPT2 knockdown neurons (Figures S6C–S6F).

We next investigated whether calcium-dependent mechanisms contribute to the activity-dependent loss of pMLC and other AIS components. In agreement with a prior report that analyzed depolarization over a longer time course (Evans et al., 2015), calcium chelation with EGTA and inhibition of L-type calcium channels with nimodipine completely prevented AIS disassembly (Figure S5D); calcium chelation likewise fully blocked loss of pMLC (Figures 6B and 6C). Several calcium-activated pathways are known to regulate AIS integrity and plasticity. These include the calpain family of calcium-dependent cysteine proteases (Ma, 2013), previously implicated in AIS disassembly during anoxia and excitotoxicity (Benned-Jensen et al., 2016; Schafer et al., 2009), and calcineurin, implicated in AIS disassembly and repositioning during prolonged depolarization (Evans et al., 2013). We found that the calpain inhibitor MDL28170 partially rescued pMLC levels and more completely rescued AnkG levels with depolarization (Figure 6D). The calcineurin inhibitor CsA reduced the levels of pMLC and AnkG to varying degrees under resting conditions (Figure S4E), which confounded interpretation of a potential rescue during depolarization (data not shown).

Together, these data suggest that rapid loss of pMLC and subsequent AIS disassembly result from several cooperative mechanisms. Activation of calpain, and likely other calcium-dependent pathways, is responsible for the loss of pMLC and other AIS components. Myosin phosphatase may also be activated with depolarization, contributing modestly to the loss of pMLC in the AIS. These results also suggest an additional function of myosin phosphatase is to suppress ectopic accumulation of pMLC and other AIS components in the distal axon during depolarization.

Stabilizing the Actin Cytoskeleton Blocks AIS Disassembly, but Not Loss of pMLC

The rapid activity-dependent loss of pMLC relative to AnkG and Nav suggests that it contributes to AIS plasticity, potentially by

destabilizing an actin-myosin II cytoskeletal scaffold in the AIS. To assess this possibility, we treated Hc neuron cultures with the membrane-permeable actin filament stabilizers phalloidin oleate and jasplakinolide (Spector et al., 1999). Treatment with phalloidin oleate completely blocked the activity-dependent loss of AnkG, but it only modestly rescued pMLC in the AIS (Figures 6E and 6G), from 73% to 116% of control ($p < 0.0001$) and 31% to 52% of control ($p = 0.0038$), respectively. A similar full rescue of AnkG, but not of pMLC, was seen with the actin stabilizer jasplakinolide during depolarization (data not shown). These results indicate that actin destabilization is a common late-stage event that underlies activity-dependent AIS disassembly. As the rescue of pMLC levels by actin stabilization was limited, pMLC turnover and a corresponding reduction of myosin II contractility are likely upstream of actin destabilization.

pMLC Is Associated with Actin Rings in the AIS

Finally, we used stochastic optical reconstruction microscopy (STORM) imaging to examine how pMLC, and thus contractile myosin II, is organized in the AIS. The AIS of a DIV10 Hc neuron, identified by epifluorescence microscopy (Figure 7A) and imaged by STORM (Figure 7B), showed overlap of the actin and pMLC labeling. Actin spacing of ~ 190 nm was evident in discrete sites along the axon (Figure 7C), consistent with the known periodicity of the actin rings. In these sites, pMLC was present as clusters that demonstrated a similar periodicity (Figure 7C) and a slight offset on the corresponding intensity scans (Figure 7D), strongly suggesting a direct association. As with epifluorescence imaging, the intensity of pMLC staining in the AIS was attenuated in the distal AIS and nearly absent along the remainder of the axon (data not shown).

In agreement with the epifluorescence imaging (Figure 5), depolarization by KCl resulted in rapid loss of pMLC, which was largely gone after 15 min of 50 mM KCl, whereas actin periodicity was relatively preserved (Figures 7E–7H). At longer time periods, KCl treatment resulted in a dramatic reorganization of actin from a periodic repeat structure to a more filamentous appearance. This reorganization was partially evident in the distal AIS at 15 min (Figure 7F), and it was robust after 30 min of KCl treatment (data not shown).

Based on these findings, we propose that pMLC/contractile myosin II associates with the periodic actin cytoskeleton to

(C) Changes in the spatial intensity profiles of pMLC (red) and AnkG (green) after 30 min of depolarization with 50 mM KCl (blue) are shown. Graphs are average intensities \pm SEM.

(D) Cumulative probability curves show near complete loss of pMLC (red) and partial loss of AnkG (green) after 30 min depolarization with 50 mM KCl (blue). Curves are calculated from all MAP2+ neurons.

(E) Burst-like light stimulation of channelrhodopsin 2 (ChR2)-infected rat Hc neurons. Staining is shown for pMLC (red) and AnkG (magenta) of control (dark, top panels) or stimulated (blue light for 15 min, bottom panels). Native fluorescence of the ChR2-Venus fusion protein is shown in green. The dotted line demarcates the partially disassembled AIS. Scale bar, 10 μ m.

(F) Changes in the spatial intensity profiles of pMLC (red) and AnkG (green) after 15 min of depolarization with a burst-like light stimulus (blue) in ChR2-expressing neurons. Graphs are average intensities \pm SEM.

(G) Total MLC intensity at the AIS does not change significantly after 30 min of depolarization with 50 mM KCl. Graph shows average intensities \pm SEM of control (black) versus depolarized (gray). Mann-Whitney test, $p > 0.05$.

(H) Western blots show pMLC, but not total MLC, levels decrease significantly after 30 min of KCl-mediated depolarization. Graphs show average intensities \pm SEM of control (black) versus depolarized neurons (gray). Values are normalized to tubulin as a loading control. Two-tailed unpaired t test, *** $p < 0.001$.

(I) Quantifications of pMLC (red) and AnkG (green) intensities after 60 min of depolarization with 50 mM KCl and a subsequent 3-hr recovery in conditioned media (5 mM KCl). Data points show average intensities \pm SEM, normalized to the corresponding non-depolarized levels. Mann-Whitney test, ** $p \leq 0.01$ and **** $p < 0.0001$. See also Figure S5.

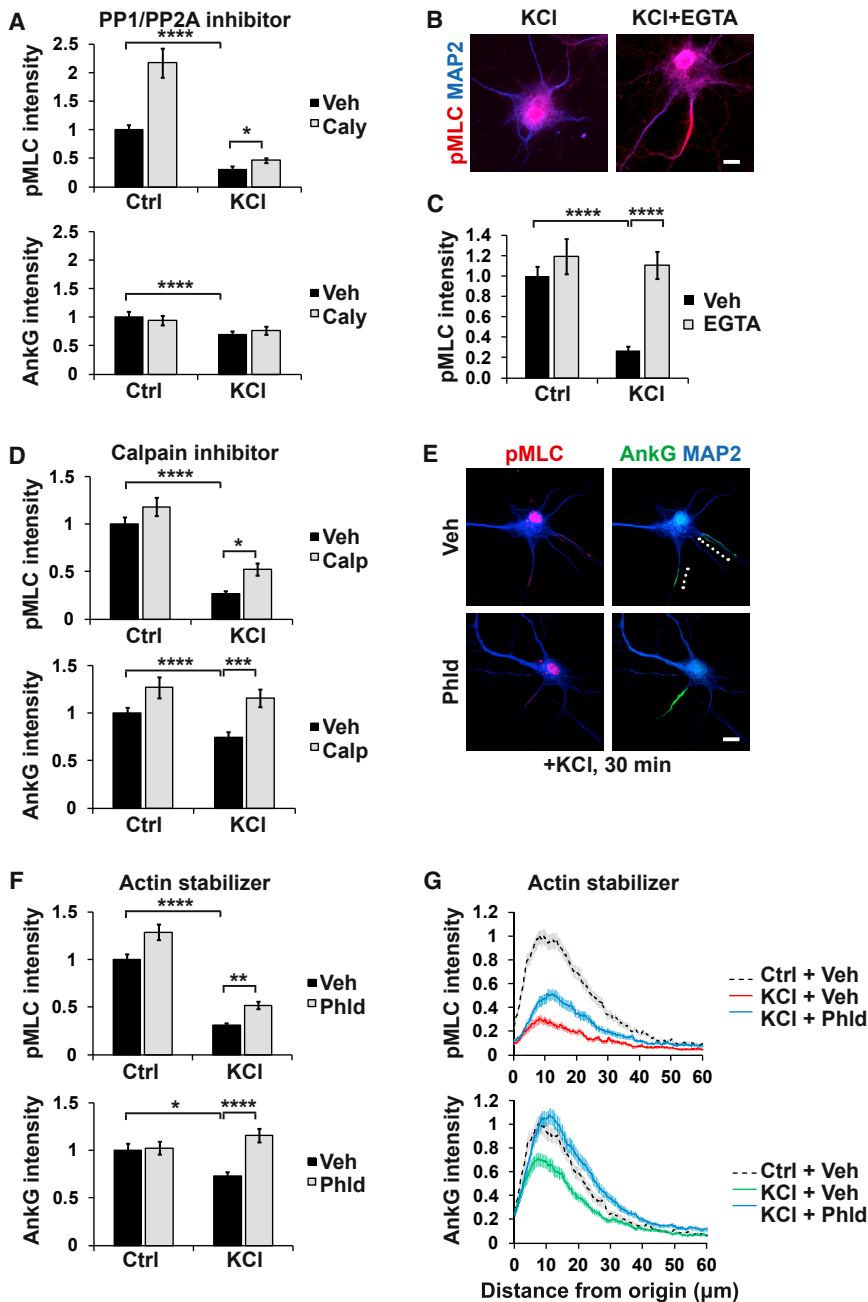


Figure 6. Mechanisms that Contribute to Depolarization-Dependent pMLC Loss and AIS Disassembly

(A) Treatment with the PP1/PP2A inhibitor calyculin A (gray) significantly increases pMLC levels (top) in control and neurons depolarized with 50 mM KCl for 30 min, relative to vehicle (veh). AnkG is not affected by calyculin treatment (bottom). Graphs show average intensities \pm SEM. Kruskal-Wallis test with Dunn's correction, $*p \leq 0.05$ and $****p < 0.0001$.

(B) Calcium chelation with 5 mM EGTA completely rescues pMLC (red) levels during depolarization with 50 mM KCl. MAP2 (blue) staining is shown. Scale bar, 10 μm .

(C) Quantification of vehicle (control; black) and EGTA (gray) treatments after depolarization with 50 mM KCl. Graphs show pMLC intensity \pm SEM. Kruskal-Wallis test with Dunn's correction, $****p < 0.0001$.

(D) Incubation with the calpain inhibitor MDL28170 (gray) partially rescues pMLC (top) and AnkG (bottom) levels during a 30-min depolarization with 50 mM KCl, relative to vehicle (black). Graphs show average intensities \pm SEM. Kruskal-Wallis test with Dunn's correction, $*p \leq 0.05$, $***p \leq 0.001$, and $****p < 0.0001$.

(E) A 1-hr preincubation with phalloidin-oleate (Phld) to stabilize actin prevents loss of AnkG (green), but not pMLC (red), with a 30-min depolarization with 50 mM KCl. MAP2 (blue) is shown. Scale bar, 10 μm .

(F) Quantification of pMLC and AnkG in the AIS, demonstrating rescue of AnkG (right), but not pMLC (left), levels after treatment with phalloidin-oleate (gray) relative to vehicle (black). Graphs show average intensities \pm SEM with 5 mM or 50 mM KCl. Kruskal-Wallis test with Dunn's correction, $*p \leq 0.05$, $**p \leq 0.01$, and $****p < 0.0001$.

(G) Spatial intensity profiles of pMLC (red, top) and AnkG (green, bottom) upon depolarization with 50 mM KCl \pm phalloidin-oleate (blue); control (non-depolarized) cultures treated with vehicle (black dashed lines) are shown for comparison. Graphs are average intensities \pm SEM and are normalized to the control peak.

See also Figure S6.

form actomyosin rings in the AIS, as shown in Figure 7I. These findings also indicate that, during early stages of AIS disassembly, pMLC is lost prior to actin destabilization.

DISCUSSION

The AIS has long been known to be linked to and dependent on the actin cytoskeleton for its function (Winckler et al., 1999). However, whether the actin cytoskeleton in the AIS is distinct from that elsewhere in the axon, potentially contributing to the proximal localization of the AnkG/ β IV spectrin complex, was

unclear. Here we show that pMLC, a marker and activator of contractile myosin II, is an early component of the AIS and of nodes of Ranvier where it associates with the periodic, submembranous actin rings. During development, MLC phosphorylation and contractile myosin II activity are essential for proper AIS assembly and regulate its distribution along the axon. Conversely, depolarization rapidly downregulates pMLC levels, destabilizing the actin cytoskeleton, which provides a mechanism for activity-dependent plasticity of the AIS. These findings suggest potential models for myosin II function in the AIS, as discussed further below.

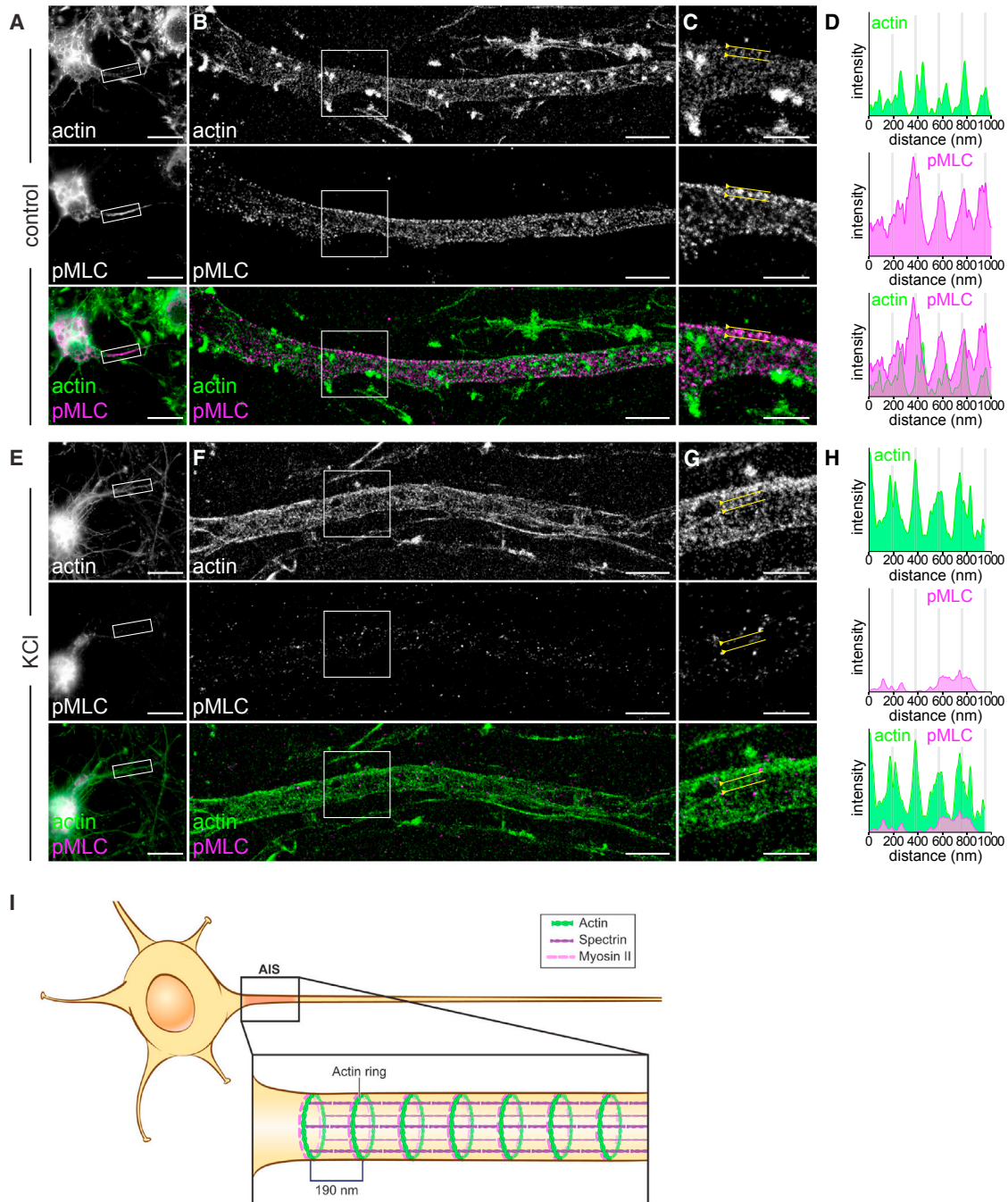


Figure 7. Nanoscale Organization of pMLC and Actin at the AIS

(A) Wide-field epifluorescence image of a control DIV10 hippocampal neuron fixed and labeled for actin (top, green on bottom overlay) and pMLC (middle, magenta on bottom overlay). Scale bar, 20 μm .

(B) STORM image of the AIS from this control neuron (boxed area in A) with actin labeling (top, green on bottom overlay) and pMLC labeling (middle, magenta on bottom overlay). Scale bar, 2 μm .

(C) Magnified region of interest (boxed area in B) with actin labeling (top, green on bottom overlay) and pMLC labeling (middle, magenta on bottom overlay). Scale bar, 1 μm .

(D) Intensity profiles along the 1- μm yellow lines highlighted in (C), showing the actin- (green) and pMLC- (magenta) labeling intensities.

(E) Wide-field epifluorescence image of a DIV10 hippocampal neuron after 15-min depolarization with 50 mM KCl, fixed and labeled for actin (top, green on bottom overlay) and pMLC (middle, magenta on bottom overlay). Scale bar, 20 μm .

(F) STORM image of the AIS from this depolarized neuron (boxed area in E) with actin labeling (top, green on bottom overlay) and pMLC labeling (middle, magenta on bottom overlay). Scale bar, 2 μm .

(legend continued on next page)

pMLC Is an Early Marker of AnkG-Based Electrogenic Domains

A striking result is that pMLC is an early marker of the AIS (Figure 2), accumulating simultaneously with AnkG, which is generally considered to be the primary nucleator of AIS assembly. pMLC is also an early component of PNS and CNS nodes based on its expression in myelinating cocultures (Figure S1D) and in the developing CNS (data not shown). Here we have focused on the function of pMLC in the AIS assembly and plasticity, which are cell-autonomous events. In contrast, nodes assemble non-cell autonomously, driven by glial contacts that first position CAMs along the axon and then recruit and localize the AnkG/spectrin complex (Dzhashiashvili et al., 2007; Zhang et al., 2012). Given the early expression of pMLC at both the AIS and nodes, and the shared molecular compositions of these electrogenic domains, it will be of interest to determine whether pMLC is also essential in node assembly and maintenance.

Regulation of pMLC Levels and Distribution

A major question is what restricts phosphorylation of MLC, and thereby contractile myosin II activity, to the proximal axon. This localization, which contrasts with the broad expression of total MLC and other myosin II subunits in neurons (Figure S2), suggests a relative abundance of kinase activity in the AIS and/or of phosphatase activity in the distal axon. Potential asymmetry in the distributions of kinase and phosphatase activities is also suggested by the developmental time course that shows pMLC is initially abundant and uniform throughout the axon (DIV2) and later increases proximally and decreases distally (Figure 2). In support of increased kinase activity in the AIS, brief pharmacological inhibition of MLCK at DIV4 substantially reduced proximal pMLC levels and flattened its distribution along the axon (Figure 3E). In contrast, brief inhibition of phosphatase activity with calyculin (Figures S4B–S4F) or sustained inhibition from genetically targeted reductions of MYPT subunits (Figure 4) increased pMLC levels in the mature AIS and distal axon, although the striking enrichment in the proximal axon persisted. Together, these results implicate elevated MLCK activity as a primary driver of pMLC enrichment in the AIS during development, and they suggest that myosin phosphatase activity is more broadly distributed. The rapid elevation of pMLC levels with a brief calyculin treatment of DIV10 Hc neurons indicates there is ongoing kinase activity in the mature AIS; the specific kinase(s) remains to be established.

A related issue is whether localization of pMLC is independent of or dictated by accumulation of the AIS complex. Treatment of developing neurons with blebbistatin, which markedly reduced AnkG, but not pMLC, levels in the AIS (Figures 3A–3C), suggests pMLC can accumulate independently of the AIS complex under some circumstances. However, the coincident spatial and temporal accumulation of pMLC and AnkG in the developing AIS (Figure 2) and the proportionate reductions of pMLC with

knockdown of AIS components (Figures S3B–S3E) strongly suggest that pMLC co-accumulates with and requires the AIS complex for stable expression. One possibility is that interactions with the AnkG/spectrin/actin complex stabilize the contractile myosin II cytoskeleton. A similar, reciprocal stabilizing effect of AIS membrane proteins on AnkG was recently reported (Letierrier et al., 2017). The AIS complex may also serve to localize MLCKs, e.g., MLCK, to this site, as has been shown for other signaling components at the AIS. These include CAMKII, which binds directly to the C-terminal tail of β IV spectrin (Hund et al., 2010), and casein kinase 2 (CK2), which interacts with NaV (Hien et al., 2014). Similarly, MLCK binds with high affinity to actin and actomyosin filaments in other cell types (Smith and Stull, 2000; Yang et al., 2006). Whether MLCK, which is homologous to CAMKII, can be localized to the proximal axon by interactions with components of the AIS is not yet known.

Phosphorylation of MLC Regulates the Assembly and Distribution of the AIS Complex

A key finding is that pMLC and myosin II activity are necessary and sufficient to initiate AIS assembly. Thus, in loss-of-function studies, inhibitors of myosin II activity (e.g., blebbistatin) and of MLC phosphorylation (e.g., the MLCK inhibitor ML7) substantially blocked the accumulation of AnkG (Figure 3) and other AIS components (e.g., NaV and NF186; data not shown). In gain-of-function studies, increasing pMLC levels by reducing myosin phosphatase activity increased AnkG levels within the AIS (Figure 4). However, the increase in pMLC was greater than that of AnkG, potentially reflecting stoichiometric constraints on AnkG recruitment to available binding sites on β IV spectrin. Notably, there were significant ectopic outposts of AnkG and other AIS components in MYPT-depleted axons, located well outside of the proximal axon (Figure 4). These latter results indicate that pMLC is sufficient to recruit and/or stabilize AIS components in regions of the axon from which it is normally excluded. They further indicate that myosin phosphatase activity, by reducing pMLC levels, normally promotes the clearance of AIS components from the distal axon during development (Figure 2).

Contractile Myosin II: Functional Organization and Role in AIS Assembly

Phosphorylation of MLC classically drives actin/myosin II contractility via two complementary functions: by promoting actin-directed ATPase activity and by assembly of actomyosin filaments (Heissler and Sellers, 2014). Diphosphorylated MLC, the form analyzed here, is thought to regulate myosin II assembly and contraction in spatially restricted locations (Watanabe et al., 2007) and to preferentially promote formation of actomyosin bundles (Vicente-Manzanares and Horwitz, 2010). Thus, diphosphorylated MLC likely promotes both myosin filament assembly and contractility in the AIS. A key question is how these functions of myosin II contribute to AIS assembly.

(G) Magnified region of interest (boxed area in F) with actin labeling (top, green on bottom overlay) and pMLC labeling (middle, magenta on bottom overlay). Scale bar, 1 μ m.

(H) Intensity profiles along the 1- μ m yellow lines highlighted in (C), showing the actin- (green) and pMLC- (magenta) labeling intensities.

(I) Schematic demonstrating proposed relationship of myosin II (magenta) and, thus, pMLC with actin rings (green) and spectrin tetramers (purple) in the AIS.

An important insight into this is provided by STORM imaging, which strongly suggests pMLC in the AIS (Figure 7) and by inference at the nodes is associated with the subcortical circumferential actin rings (Leterrier et al., 2015; Xu et al., 2013). Based on this nanoscale organization, pMLC is unlikely to interact directly with the subcortical actin patches identified by live imaging (D'Este et al., 2015; Watanabe et al., 2012) or with the dynamic, longitudinal actin filaments present in the interior of axons (Ganguly et al., 2015; Xu et al., 2013). pMLC regulates the head groups of the heavy chains of the hexameric myosin II complex (Heissler and Sellers, 2014), which likely mediate the binding of myosin II to the actin rings. Myosin II is further organized into bipolar filaments as the result of hydrophobic interactions of the C-terminal tails of the heavy chains (Vicente-Manzanares et al., 2009). Given their functional organization with actin (Vicente-Manzanares et al., 2009), it is likely that myosin II filaments are oriented parallel to the actin rings. An alternative formal possibility is that the myosin II filaments extend between these rings. However, this would require the pMLC/myosin II filaments, which are ~300 nm in length (Billington et al., 2013), to be obliquely oriented to accommodate the 190 nm spacing between actin rings, and, therefore, seems less likely. In the future, super-resolution imaging of different domains of the myosin II filaments (e.g., the head and tail regions) will be useful to establish the precise orientation of these filaments relative to the actin rings.

Thus, we suggest that actin and contractile myosin II in the AIS form contractile actomyosin rings (Figure 7I), representing a novel mechanism for regulating actin in the proximal axon and nodes of Ranvier distinct from that in the remainder of the axon. Actin rings are widespread throughout phylogeny and are comprised of F-actin, parallel myosin II filaments (Henson et al., 2017), and actin-modifying proteins that regulate their contractility and organization (Schwayer et al., 2016). They have well-described roles functioning to either constrict cellular structures via myosin II motor activity, notably the fission apparatus during cytokinesis, or alternatively to stabilize cytoskeletal and adhesion complexes, notably at intercellular junctions (Schwayer et al., 2016).

Actomyosin rings may promote AIS assembly via several mechanisms. Analogous to its function at cell contact sites, including adherens junctions and at other non-motile cytoskeletal apparatuses (Ma and Adelstein, 2014; Schwayer et al., 2016), myosin II activity in the rings may generate tension on the spectrin/ankyrin cytoskeleton. The site of maximal contractile activity is expected to be the central AIS, where pMLC and other components of the AIS (e.g., AnkG and NaV) are most abundant. Tension on the actin rings may, in turn, result in mechanosensitive changes of the AIS cytoskeleton that drives the assembly, stability, and/or recruitment of conformationally dependent interacting proteins, akin to that described at adherens junctions (Ladoux et al., 2015). More speculatively, tension could drive mechanotransduction that affects the organization and recruitment of actin-associated protein-signaling complexes (Newell-Litwa et al., 2015) at the AIS, similar to signaling at focal adhesions (Provenzano and Keely, 2011; Zaidel-Bar et al., 2015). Finally, myosin II activity may promote assembly of the actin rings (Miyazaki et al., 2015), which first assemble in the proximal axon approximately coincident with or just after robust accumu-

lation of pMLC, i.e., ~DIV5 (Zhong et al., 2014). The actin rings in the proximal axon are themselves a scaffold that organizes and potentially stabilizes the AIS cytoskeleton. Elucidating which of these roles of myosin II are responsible for promoting AIS assembly and stability will be of considerable interest for future studies.

pMLC Is a Key Target of Activity-Dependent AIS Plasticity

We have found activity-dependent remodeling of the AIS to be even more rapid and general than previously appreciated (Evans et al., 2015). Thus, just 15 min of optogenetic stimulation and 30 min of KCl treatment were sufficient to reduce the levels of AnkG across the AIS in all MAP2+ Hc neurons (Figure 5). The loss of pMLC with KCl treatment was particularly striking; it is far more rapid (i.e., within 5 min) and more extensive than that of any other AIS component in our studies (Figures 5B and S5) or reported to date.

pMLC loss triggered by depolarization results from multiple mechanisms initiated by calcium influx, including a modest degree of dephosphorylation (Figure 6A) and calpain-mediated proteolysis (Figure 6D). pMLC is uniquely sensitive to calpain compared to total MLC (Figures 5G and 5H), potentially due to its phosphorylation-dependent conformation (Heissler and Sellers, 2014). Our data also suggest that calpain-dependent proteolysis contributes to the degradation of other AIS components, as pMLC was partially protected whereas AnkG was completely protected by calpain inhibition (Figure 6D). Indeed, multiple AIS components, including AnkG, Nav1.2, NF186, and β IV and other spectrins (Ma, 2013), are known targets of calpain during anoxic injury (Schafer et al., 2009) and excitotoxicity (Benned-Jensen et al., 2016). Thus, calcium-dependent effects on multiple AIS components likely cumulatively destabilize the AIS. Whether other components of the myosin II hexamer are also affected by depolarization and contribute to disruption of myosin II and the AIS will be of interest for further study.

A key question is how the rapid loss of pMLC might contribute to activity-dependent AIS plasticity. We have shown that pMLC loss precedes actin disorganization, based on STORM imaging (Figure 7), and that pharmacologically stabilizing the actin cytoskeleton completely protects the AIS, but not pMLC, from disassembly (Figures 6F and 6G). These results indicate that actin destabilization is a common final pathway of upstream calcium-dependent signals. Loss of pMLC, which would be expected to disrupt actin filaments either via loss of contractile myosin II activity and/or of myosin filaments (Park et al., 2011), is a likely candidate to initiate these events. A recent report proposes that myosin II contractility destabilizes the AIS during depolarization (Evans et al., 2017), as suggested by the demonstration that short-term blebbistatin treatment protects the AIS from activity-induced disassembly, a finding we have corroborated (S.L.B. and J.L.S., unpublished data). This unexpected effect of blebbistatin likely reflects instead its paradoxical ability to stabilize actin filaments during short-term incubations (Haviv et al., 2008), as myosin II persistently binds to and cross-links actin in the presence of blebbistatin (Kovács et al., 2004). These results are, therefore, consistent with the notion that the primary function of myosin II in the proximal axon is to stabilize actin and the AIS cytoskeleton.

Taken together, we propose the activity-dependent loss of pMLC primarily destabilizes the actin cytoskeleton by disrupting myosin II filaments that stabilize the actin rings (Figure 7E). Disruption of myosin II filaments from loss of pMLC, together with calpain-mediated proteolysis of other AIS components (Figure 6D), may act as coincidence detectors that cooperatively destabilize the entire AIS complex.

AIS Disassembly and Homeostatic Plasticity

Several forms of AIS plasticity with differing time courses have been described. *In vivo*, deafferentation or reduced activity lengthens the AIS, rendering the neuron more likely to fire action potentials (Yamada and Kuba, 2016). Conversely, hyperactivation of neurons, largely modeled by depolarization of Hc neurons *in vitro* (Grubb and Burrone, 2010) and in slice cultures (Wefelmeyer et al., 2015), shifts the AIS away from the soma over 48 hr, reducing excitability. Hyperactivation resulting from seizure activity similarly shortens and displaces the AIS *in vivo* (Liu et al., 2017).

What is the relationship of the rapid disassembly of the AIS described here with sustained activity to the spatial alterations in the length and location of the AIS seen over longer time periods *in vivo*? Changes in the position of the AIS observed *in vivo* have been proposed to result from partial repetitive cycles of disassembly and reassembly (Kuba et al., 2014). In agreement, we observed that loss of pMLC and AnkG in the AIS following depolarization is accompanied by a significant accumulation of these, and other AIS components, in the distal axon, particularly in MYPT-deficient neurons (Figure S6). These results, which suggest AIS disassembly mobilizes components for recruitment and reassembly in the axon, provide a potential mechanism for AIS relocation. The activity-dependent increase of pMLC in the distal axon (Figure S6), driven either by inactivation of myosin phosphatase and/or activation of calcium/calmodulin-dependent MLCK (Heissler and Sellers, 2014), is a candidate to promote this relocation.

These findings further underscore the AIS as a locus of dynamic activity-dependent plasticity. They highlight pMLC/myosin II as a new component of the AIS cytoskeleton required for its assembly and a key substrate of plasticity. The importance of pMLC and myosin II in generating and stabilizing the AIS also raises the possibility that they are important disease targets as well. Indeed, the AIS has emerged as a pathological target in a diverse group of neurological disorders (Buffington and Rasband, 2011; Leterrier, 2016). Additional studies of the regulation, organization, and pathology of myosin II in the AIS promise to provide new insights into these disorders.

STAR★METHODS

Detailed methods are provided in the online version of this paper and include the following:

- KEY RESOURCES TABLE
- CONTACT FOR REAGENT AND RESOURCE SHARING
- EXPERIMENTAL MODEL AND SUBJECT DETAILS
 - Primary Neuron Cultures from E18 Rat Hippocampus and Cortex

- Conditional MYPT1 Knockout Mice
- Primary Neuron Cultures from E18 Mouse Hippocampus and Cortex

● METHOD DETAILS

- MYPT1 Knockout Experiments
- Lentiviral Knockdown Experiments
- Pharmacology and Depolarization Experiments
- Optogenetic Stimulation of Cultured Neurons
- Immunofluorescence of Neuronal Cultures
- Imaging of Cultured Neurons
- Imaging of Nerve and Mouse Brain Sections
- RNA Expression Experiments
- Western Blots
- Phosphatase Treatment of Cultured Neurons
- 2D STORM Imaging

● QUANTIFICATION AND STATISTICAL ANALYSIS

- Quantitative AIS Image Analysis
- Statistical Analysis and Graphing of Data

● DATA AND SOFTWARE AVAILABILITY

SUPPLEMENTAL INFORMATION

Supplemental Information includes six figures and three tables and can be found with this article online at <https://doi.org/10.1016/j.neuron.2017.12.039>.

ACKNOWLEDGMENTS

We thank M. Bhat and M. Rasband for generously providing antibodies, D. Wansink for providing GFP-tagged MLC constructs, J. Stull and J. Sellers for helpful discussions, M. Long for advice on optogenetic studies, G. Fishell and R. Tsien for comments on the manuscript, and J. Gregory for artwork. This research was supported by grants from the NIH (NS043474) and the National Multiple Sclerosis Society (RG 4748-A-13). S.L.B. is an MSTP trainee supported by the NYU NIH MSTP training grant (T32 GM007308).

AUTHOR CONTRIBUTIONS

Conceptualization, S.L.B. and J.L.S.; Methodology, S.L.B., A.L.-M., S.Y., Y.Z., L.K., E.A.-P., M.-S.Z., E.R., M.D., G.C., C.L., and J.L.S.; Validation, S.L.B., A.L.-M., and S.Y.; Formal Analysis, S.L.B., A.L.-M., and S.Y.; Investigation, S.L.B., A.L.-M., S.Y., S.P., Y.Z., E.A.-P., G.C., L.K., and C.V.M.-V.; Resources, S.L.B., A.L.-M., S.Y., S.P., Y.Z., E.A.-P., M.-S.Z., E.R., and M.D.; Writing – Original Draft, S.L.B. and J.L.S.; Writing – Review & Editing, S.L.B., A.L.-M., S.Y., E.R., C.V.M.-V., M.D., and J.L.S.; Visualization, S.L.B., S.Y., and J.L.S.; Supervision, E.R., M.D., C.L., and J.L.S.; Funding Acquisition, J.L.S.

DECLARATION OF INTERESTS

The authors declare no competing interests.

Received: March 6, 2017

Revised: August 24, 2017

Accepted: December 22, 2017

Published: January 25, 2018

REFERENCES

- Bender, K.J., and Trussell, L.O. (2012). The physiology of the axon initial segment. *Annu. Rev. Neurosci.* 35, 249–265.
- Benned-Jensen, T., Christensen, R.K., Denti, F., Perrier, J.F., Rasmussen, H.B., and Olesen, S.P. (2016). Live Imaging of Kv7.2/7.3 cell surface dynamics at the axon initial segment: high steady-state stability and calpain-dependent excitotoxic downregulation revealed. *J. Neurosci.* 36, 2261–2266.

- Bennett, V., and Lorenzo, D.N. (2016). An adaptable spectrin/ankyrin-based mechanism for long-range organization of plasma membranes in vertebrate tissues. *Curr. Top. Membr.* **77**, 143–184.
- Billington, N., Wang, A., Mao, J., Adelstein, R.S., and Sellers, J.R. (2013). Characterization of three full-length human nonmuscle myosin II paralogs. *J. Biol. Chem.* **288**, 33398–33410.
- Brown, J., and Bridgman, P.C. (2003). Role of myosin II in axon outgrowth. *J. Histochem. Cytochem.* **51**, 421–428.
- Brown, M.E., and Bridgman, P.C. (2004). Myosin function in nervous and sensory systems. *J. Neurobiol.* **58**, 118–130.
- Buffington, S.A., and Rasband, M.N. (2011). The axon initial segment in nervous system disease and injury. *Eur. J. Neurosci.* **34**, 1609–1619.
- D'Este, E., Kamin, D., Göttfert, F., El-Hady, A., and Hell, S.W. (2015). STED nanoscopy reveals the ubiquity of subcortical cytoskeleton periodicity in living neurons. *Cell Rep.* **10**, 1246–1251.
- D'Este, E., Kamin, D., Velte, C., Göttfert, F., Simons, M., and Hell, S.W. (2016). Subcortical cytoskeleton periodicity throughout the nervous system. *Sci. Rep.* **6**, 22741.
- Davis, L., Abdi, K., Machius, M., Brautigam, C., Tomchick, D.R., Bennett, V., and Michaely, P. (2009). Localization and structure of the ankyrin-binding site on beta2-spectrin. *J. Biol. Chem.* **284**, 6982–6987.
- Dotti, C.G., Sullivan, C.A., and Banker, G.A. (1988). The establishment of polarity by hippocampal neurons in culture. *J. Neurosci.* **8**, 1454–1468.
- Dzhashiashvili, Y., Zhang, Y., Galinska, J., Lam, I., Grumet, M., and Salzer, J.L. (2007). Nodes of Ranvier and axon initial segments are ankyrin G-dependent domains that assemble by distinct mechanisms. *J. Cell Biol.* **177**, 857–870.
- Evans, M.D., Sammons, R.P., Lebron, S., Dumitrescu, A.S., Watkins, T.B., Uebele, V.N., Renger, J.J., and Grubb, M.S. (2013). Calcineurin signaling mediates activity-dependent relocation of the axon initial segment. *J. Neurosci.* **33**, 6950–6963.
- Evans, M.D., Dumitrescu, A.S., Kruijssen, D.L.H., Taylor, S.E., and Grubb, M.S. (2015). Rapid modulation of axon initial segment length influences repetitive spike firing. *Cell Rep.* **13**, 1233–1245.
- Evans, M.D., Tufo, C., Dumitrescu, A.S., and Grubb, M.S. (2017). Myosin II activity is required for structural plasticity at the axon initial segment. *Eur. J. Neurosci.* **46**, 1751–1757.
- Flynn, K.C., Pak, C.W., Shaw, A.E., Bradke, F., and Bamberg, J.R. (2009). Growth cone-like waves transport actin and promote axonogenesis and neurite branching. *Dev. Neurobiol.* **69**, 761–779.
- Fréal, A., Fassier, C., Le Bras, B., Bullier, E., De Gois, S., Hazan, J., Hoogenraad, C.C., and Couraud, F. (2016). Cooperative interactions between 480 kDa Ankyrin-G and EB proteins assemble the axon initial segment. *J. Neurosci.* **36**, 4421–4433.
- Galiano, M.R., Jha, S., Ho, T.S., Zhang, C., Ogawa, Y., Chang, K.J., Stankewich, M.C., Mohler, P.J., and Rasband, M.N. (2012). A distal axonal cytoskeleton forms an intra-axonal boundary that controls axon initial segment assembly. *Cell* **149**, 1125–1139.
- Ganguly, A., Tang, Y., Wang, L., Ladit, K., Loi, J., Dargent, B., Leterrier, C., and Roy, S. (2015). A dynamic formin-dependent deep F-actin network in axons. *J. Cell Biol.* **210**, 401–417.
- Grassie, M.E., Moffat, L.D., Walsh, M.P., and MacDonald, J.A. (2011). The myosin phosphatase targeting protein (MYPT) family: a regulated mechanism for achieving substrate specificity of the catalytic subunit of protein phosphatase type 1 δ . *Arch. Biochem. Biophys.* **510**, 147–159.
- Greer, P.L., and Greenberg, M.E. (2008). From synapse to nucleus: calcium-dependent gene transcription in the control of synapse development and function. *Neuron* **59**, 846–860.
- Grubb, M.S., and Burrone, J. (2010). Activity-dependent relocation of the axon initial segment fine-tunes neuronal excitability. *Nature* **465**, 1070–1074.
- Haviv, L., Gillo, D., Backouche, F., and Bernheim-Groswasser, A. (2008). A cytoskeletal demolition worker: myosin II acts as an actin depolymerization agent. *J. Mol. Biol.* **375**, 325–330.
- He, W.Q., Qiao, Y.N., Peng, Y.J., Zha, J.M., Zhang, C.H., Chen, C., Chen, C.P., Wang, P., Yang, X., Li, C.J., et al. (2013). Altered contractile phenotypes of intestinal smooth muscle in mice deficient in myosin phosphatase target subunit 1. *Gastroenterology* **144**, 1456–1465.
- He, J., Zhou, R., Wu, Z., Carrasco, M.A., Kurshan, P.T., Farley, J.E., Simon, D.J., Wang, G., Han, B., Hao, J., et al. (2016). Prevalent presence of periodic actin-spectrin-based membrane skeleton in a broad range of neuronal cell types and animal species. *Proc. Natl. Acad. Sci. USA* **113**, 6029–6034.
- Hedstrom, K.L., Xu, X., Ogawa, Y., Frischknecht, R., Seidenbecher, C.I., Shrager, P., and Rasband, M.N. (2007). Neurofascin assembles a specialized extracellular matrix at the axon initial segment. *J. Cell Biol.* **178**, 875–886.
- Hedstrom, K.L., Ogawa, Y., and Rasband, M.N. (2008). AnkyrinG is required for maintenance of the axon initial segment and neuronal polarity. *J. Cell Biol.* **183**, 635–640.
- Heissler, S.M., and Sellers, J.R. (2014). Myosin light chains: teaching old dogs new tricks. *Bioarchitecture* **4**, 169–188.
- Henson, J.H., Ditzler, C.E., Germain, A., Irwin, P.M., Vogt, E.T., Yang, S., Wu, X., and Shuster, C.B. (2017). The ultrastructural organization of actin and myosin II filaments in the contractile ring: new support for an old model of cytokinesis. *Mol. Biol. Cell* **28**, 613–623.
- Hien, Y.E., Montersino, A., Castets, F., Leterrier, C., Filhol, O., Vacher, H., and Dargent, B. (2014). CK2 accumulation at the axon initial segment depends on sodium channel Nav1. *FEBS Lett.* **588**, 3403–3408.
- Hirano, M., and Hirano, K. (2016). Myosin di-phosphorylation and peripheral actin bundle formation as initial events during endothelial barrier disruption. *Sci. Rep.* **6**, 20989.
- Hund, T.J., Koval, O.M., Li, J., Wright, P.J., Qian, L., Snyder, J.S., Gudmundsson, H., Kline, C.F., Davidson, N.P., Cardona, N., et al. (2010). A β (IV)-spectrin/CaMKII signaling complex is essential for membrane excitability in mice. *J. Clin. Invest.* **120**, 3508–3519.
- Jenkins, S.M., and Bennett, V. (2001). Ankyrin-G coordinates assembly of the spectrin-based membrane skeleton, voltage-gated sodium channels, and L1 CAMs at Purkinje neuron initial segments. *J. Cell Biol.* **155**, 739–746.
- Kato, Y., Fusetani, N., Matsunaga, S., and Hashimoto, K. (1988). Calyculins, potent antitumor metabolites from the marine sponge *Discodermia calyx*: biological activities. *Drugs Exp. Clin. Res.* **14**, 723–728.
- King, A.N., Manning, C.F., and Trimmer, J.S. (2014). A unique ion channel clustering domain on the axon initial segment of mammalian neurons. *J. Comp. Neurol.* **522**, 2594–2608.
- Kole, M.H., and Stuart, G.J. (2012). Signal processing in the axon initial segment. *Neuron* **73**, 235–247.
- Kollins, K.M., Hu, J., Bridgman, P.C., Huang, Y.Q., and Gallo, G. (2009). Myosin-II negatively regulates minor process extension and the temporal development of neuronal polarity. *Dev. Neurobiol.* **69**, 279–298.
- Kovács, M., Tóth, J., Hetényi, C., Málnási-Csizmadia, A., and Sellers, J.R. (2004). Mechanism of blebbistatin inhibition of myosin II. *J. Biol. Chem.* **279**, 35557–35563.
- Kuba, H., Adachi, R., and Ohmori, H. (2014). Activity-dependent and activity-independent development of the axon initial segment. *J. Neurosci.* **34**, 3443–3453.
- Ladoux, B., Nelson, W.J., Yan, J., and Mège, R.M. (2015). The mechanotransduction machinery at work at adherens junctions. *Integr. Biol.* **7**, 1109–1119.
- Leterrier, C. (2016). The axon initial segment, 50 years later: a nexus for neuronal organization and function. *Curr. Top. Membr.* **77**, 185–233.
- Leterrier, C., Potier, J., Caillol, G., Debarnot, C., Rueda Boroni, F., and Dargent, B. (2015). Nanoscale architecture of the axon initial segment reveals an organized and robust scaffold. *Cell Rep.* **13**, 2781–2793.
- Leterrier, C., Clerc, N., Rueda-Boroni, F., Montersino, A., Dargent, B., and Castets, F. (2017). Ankyrin G membrane partners drive the establishment and maintenance of the axon initial segment. *Front. Cell. Neurosci.* **11**, 6.

- Liu, T.T., Feng, L., Liu, H.F., Shu, Y., and Xiao, B. (2017). Altered axon initial segment in hippocampal newborn neurons, associated with recurrence of temporal lobe epilepsy in rats. *Mol. Med. Rep.* *16*, 3169–3178.
- Lorenzo, D.N., Badea, A., Davis, J., Hostettler, J., He, J., Zhong, G., Zhuang, X., and Bennett, V. (2014). A PI3K3C3-ankyrin-B-dynactin pathway promotes axonal growth and multiorganelle transport. *J. Cell Biol.* *207*, 735–752.
- Ma, M. (2013). Role of calpains in the injury-induced dysfunction and degeneration of the mammalian axon. *Neurobiol. Dis.* *60*, 61–79.
- Ma, X., and Adelstein, R.S. (2014). The role of vertebrate nonmuscle Myosin II in development and human disease. *Bioarchitecture* *4*, 88–102.
- Miyazaki, M., Chiba, M., Eguchi, H., Ohki, T., and Ishiwata, S. (2015). Cell-sized spherical confinement induces the spontaneous formation of contractile actomyosin rings in vitro. *Nat. Cell Biol.* *17*, 480–489.
- Newell-Litwa, K.A., Horwitz, R., and Lamers, M.L. (2015). Non-muscle myosin II in disease: mechanisms and therapeutic opportunities. *Dis. Model. Mech.* *8*, 1495–1515.
- Ovesný, M., Křížek, P., Borkovec, J., Svindrych, Z., and Hagen, G.M. (2014). ThunderSTORM: a comprehensive ImageJ plug-in for PALM and STORM data analysis and super-resolution imaging. *Bioinformatics* *30*, 2389–2390.
- Park, I., Han, C., Jin, S., Lee, B., Choi, H., Kwon, J.T., Kim, D., Kim, J., Lifirsu, E., Park, W.J., et al. (2011). Myosin regulatory light chains are required to maintain the stability of myosin II and cellular integrity. *Biochem. J.* *434*, 171–180.
- Provenzano, P.P., and Keely, P.J. (2011). Mechanical signaling through the cytoskeleton regulates cell proliferation by coordinated focal adhesion and Rho GTPase signaling. *J. Cell Sci.* *124*, 1195–1205.
- Rios, J.C., Melendez-Vasquez, C.V., Einheber, S., Lustig, M., Grumet, M., Hemperly, J., Peles, E., and Salzer, J.L. (2000). Contactin-associated protein (Casp) and contactin form a complex that is targeted to the paranodal junctions during myelination. *J. Neurosci.* *20*, 8354–8364.
- Rubinson, D.A., Dillon, C.P., Kwiatkowski, A.V., Sievers, C., Yang, L., Kopinja, J., Rooney, D.L., Zhang, M., Ihrig, M.M., McManus, M.T., et al. (2003). A lentivirus-based system to functionally silence genes in primary mammalian cells, stem cells and transgenic mice by RNA interference. *Nat. Genet.* *33*, 401–406.
- Saitoh, M., Ishikawa, T., Matsushima, S., Naka, M., and Hidaka, H. (1987). Selective inhibition of catalytic activity of smooth muscle myosin light chain kinase. *J. Biol. Chem.* *262*, 7796–7801.
- Salomon, J., Gaston, C., Magescas, J., Duvauchelle, B., Canioni, D., Sengmanivong, L., Mayeux, A., Michaux, G., Campeotto, F., Lemale, J., et al. (2017). Contractile forces at tricellular contacts modulate epithelial organization and monolayer integrity. *Nat. Commun.* *8*, 13998.
- Samanta, J., Grund, E.M., Silva, H.M., Lafaille, J.J., Fishell, G., and Salzer, J.L. (2015). Inhibition of Gli1 mobilizes endogenous neural stem cells for remyelination. *Nature* *526*, 448–452.
- Schafer, D.P., Jha, S., Liu, F., Akella, T., McCullough, L.D., and Rasband, M.N. (2009). Disruption of the axon initial segment cytoskeleton is a new mechanism for neuronal injury. *J. Neurosci.* *29*, 13242–13254.
- Schwayer, C., Sikora, M., Slovák, J., Kardos, R., and Heisenberg, C.P. (2016). Actin rings of power. *Dev. Cell* *37*, 493–506.
- Sellers, J.R. (2000). Myosins: a diverse superfamily. *Biochim. Biophys. Acta* *1496*, 3–22.
- Smith, L., and Stull, J.T. (2000). Myosin light chain kinase binding to actin filaments. *FEBS Lett.* *480*, 298–300.
- Sobotzik, J.M., Sie, J.M., Politi, C., Del Turco, D., Bennett, V., Deller, T., and Schultz, C. (2009). AnkyrinG is required to maintain axo-dendritic polarity in vivo. *Proc. Natl. Acad. Sci. USA* *106*, 17564–17569.
- Spector, I., Braet, F., Shochet, N.R., and Bubb, M.R. (1999). New anti-actin drugs in the study of the organization and function of the actin cytoskeleton. *Microsc. Res. Tech.* *47*, 18–37.
- Straight, A.F., Cheung, A., Limouze, J., Chen, I., Westwood, N.J., Sellers, J.R., and Mitchison, T.J. (2003). Dissecting temporal and spatial control of cytokinesis with a myosin II inhibitor. *Science* *299*, 1743–1747.
- Tapia, M., Wandosell, F., and Garrido, J.J. (2010). Impaired function of HDAC6 slows down axonal growth and interferes with axon initial segment development. *PLoS ONE* *5*, e12908.
- Uehata, M., Ishizaki, T., Satoh, H., Ono, T., Kawahara, T., Morishita, T., Tamakawa, H., Yamagami, K., Inui, J., Maekawa, M., and Narumiya, S. (1997). Calcium sensitization of smooth muscle mediated by a Rho-associated protein kinase in hypertension. *Nature* *389*, 990–994.
- Vicente-Manzanares, M., and Horwitz, A.R. (2010). Myosin light chain mono- and di-phosphorylation differentially regulate adhesion and polarity in migrating cells. *Biochem. Biophys. Res. Commun.* *402*, 537–542.
- Vicente-Manzanares, M., Ma, X., Adelstein, R.S., and Horwitz, A.R. (2009). Non-muscle myosin II takes centre stage in cell adhesion and migration. *Nat. Rev. Mol. Cell Biol.* *10*, 778–790.
- Wang, Y., Zhang, P., and Wyskiel, D.R. (2016). Chandelier cells in functional and dysfunctional neural circuits. *Front. Neural Circuits* *10*, 33.
- Watanabe, T., Hosoya, H., and Yonemura, S. (2007). Regulation of myosin II dynamics by phosphorylation and dephosphorylation of its light chain in epithelial cells. *Mol. Biol. Cell* *18*, 605–616.
- Watanabe, K., Al-Bassam, S., Miyazaki, Y., Wandless, T.J., Webster, P., and Arnold, D.B. (2012). Networks of polarized actin filaments in the axon initial segment provide a mechanism for sorting axonal and dendritic proteins. *Cell Rep.* *2*, 1546–1553.
- Wefelmeyer, W., Cattaert, D., and Burrone, J. (2015). Activity-dependent mismatch between axo-axonic synapses and the axon initial segment controls neuronal output. *Proc. Natl. Acad. Sci. USA* *112*, 9757–9762.
- Winckler, B., Forscher, P., and Mellman, I. (1999). A diffusion barrier maintains distribution of membrane proteins in polarized neurons. *Nature* *397*, 698–701.
- Xu, K., Zhong, G., and Zhuang, X. (2013). Actin, spectrin, and associated proteins form a periodic cytoskeletal structure in axons. *Science* *339*, 452–456.
- Yamada, R., and Kuba, H. (2016). Structural and functional plasticity at the axon initial segment. *Front. Cell. Neurosci.* *10*, 250.
- Yang, C.X., Chen, H.Q., Chen, C., Yu, W.P., Zhang, W.C., Peng, Y.J., He, W.Q., Wei, D.M., Gao, X., and Zhu, M.S. (2006). Microfilament-binding properties of N-terminal extension of the isoform of smooth muscle long myosin light chain kinase. *Cell Res.* *16*, 367–376.
- Zaidel-Bar, R., Zhenhuan, G., and Luxenburg, C. (2015). The contractome—a systems view of actomyosin contractility in non-muscle cells. *J. Cell Sci.* *128*, 2209–2217.
- Zhang, C., and Rasband, M.N. (2016). Cytoskeletal control of axon domain assembly and function. *Curr. Opin. Neurobiol.* *39*, 116–121.
- Zhang, F., Wang, L.P., Boyden, E.S., and Deisseroth, K. (2006). Channelrhodopsin-2 and optical control of excitable cells. *Nat. Methods* *3*, 785–792.
- Zhang, Y., Bekku, Y., Dzhashiashvili, Y., Armenti, S., Meng, X., Sasaki, Y., Milbrandt, J., and Salzer, J.L. (2012). Assembly and maintenance of nodes of ranvier rely on distinct sources of proteins and targeting mechanisms. *Neuron* *73*, 92–107.
- Zhong, G., He, J., Zhou, R., Lorenzo, D., Babcock, H.P., Bennett, V., and Zhuang, X. (2014). Developmental mechanism of the periodic membrane skeleton in axons. *eLife* *3*, e04581.

STAR★METHODS

KEY RESOURCES TABLE

REAGENT or RESOURCE	SOURCE	IDENTIFIER
Antibodies		
Rabbit anti-phospho-MLC 2 (Thr18/Ser19)	Cell Signaling Technology	Cat#3674; RRID: AB_2147464
Mouse anti-ankyrin G, clone 463	Santa Cruz	Cat#sc-12719; RRID: AB_626674
Chicken anti-microtubule associated protein 2	Encor	Cat#CPCA-MAP2; RRID: AB_2138173
Rabbit anti-MLC 2 (Myl9)	Cell Signaling Technology	Cat#3672; RRID: AB_330278
Rabbit anti-MLC 2 (Myl9), clone EPR13012(2)	Abcam	Cat#ab191393; RRID: AB_2721112
Rabbit anti-non-muscle MHC IIA	Covance	Cat#PRB-440; RRID: AB_291638
Rabbit anti-non-muscle MHC IIB	Covance	Cat#PRB-445; RRID: AB_291639
Rabbit anti-non-muscle MHC IIC	Covance	Cat#PRB-444; RRID: AB_2028814
Rabbit anti-Myl6 (myosin essential light chain)	Bioss	Cat#bs-4129R; RRID: AB_11091498
Goat anti-green fluorescent protein	ABD Serotec	Cat#AHP975; RRID: AB_566990
Mouse anti-tau, clone TAU-5	BD Biosciences	Cat#556319; RRID: AB_396358
Mouse anti-beta IV spectrin, clone N393/2	Neuromab	Cat#73-376; RRID: AB_2315816
Mouse anti-ankyrin G, clone N106/36	Neuromab	Cat#75-146; RRID: AB_10673030
Mouse anti-neurofascin extracellular domain, clone A12/18	Neuromab	Cat# 75-172; RRID: AB_2282826
Mouse anti-Kv2.1, clone K89/34	Neuromab	Cat# 75-014; RRID: AB_10673392
Mouse anti-sodium channel, pan, clone K58/35	Sigma	Cat#S8809; RRID:AB_477552
Chicken anti-myelin basic protein	Millipore	Cat#AB9348; RRID: AB_2140366
Guinea pig anti-Caspr	Gift of Dr. M. Bhat, UT Health San Antonio	RRID: AB_2314219
Rabbit anti-beta IV spectrin	Gift of Dr. M. Rasband, Baylor College of Medicine	RRID: AB_2315634
Bacterial and Virus Strains		
AAV1-CMV-HI-eGFP-Cre-WPRE-SV40	University of Pennsylvania Vector Core	Cat#AV-1-PV2004
AAV1-CMV-PI-eGFP-WPRE-bGH	University of Pennsylvania Vector Core	Cat#AV-1-PV0101
AAV1-CAG-ChR2-Venus	SignaGen	Cat#SL100846
Chemicals, Peptides, and Recombinant Proteins		
(-)-Blebbistatin, myosin ATPase inhibitor	Sigma	Cat#B0560
ML7 hydrochloride, MLCK inhibitor	Sigma	Cat#I2764
Y27632 dihydrochloride, ROCK inhibitor	Sigma	Cat#Y0503
SNS-314 mesylate, Aurora kinase B inhibitor	Selleck	Cat#S1154
KN-93, CaMKII inhibitor	Sigma	Cat#K1385
Tetrabromobenzotriazole (TBB), CK2 inhibitor	Tocris	Cat#2275
SC-514, I κ B kinase inhibitor	Tocris	Cat#3318
KT-5720, PKA inhibitor	Tocris	Cat#1288
Calyculin A, PP1/PP2A inhibitor	Sigma	Cat#C5552
Okadaic acid ammonium salt, PP1/PP2A inhibitor	Sigma	Cat#O8010
Fostriecin sodium salt, PP2A inhibitor	Sigma	Cat#F4425
Cyclosporin A, calcineurin inhibitor	Sigma	Cat#C1832
FK506 monohydrate, calcineurin inhibitor	Sigma	Cat#F4679
MDL 28170, calpain inhibitor	Tocris	Cat#1146
Phalloidin oleate, actin stabilizer	Sigma	Cat#P9992

(Continued on next page)

Continued

REAGENT or RESOURCE	SOURCE	IDENTIFIER
Jasplakinolide, actin stabilizer	Santa Cruz	Cat#sc-202191
Phalloidin-Atto488	Sigma	Cat#49409
Nimodipine, L-type CaV blocker	Sigma	Cat#N149
Lambda protein phosphatase with PMP buffer	New England Biolabs	Cat#P0753
Calf intestinal alkaline phosphatase	New England Biolabs	Cat#M0290
NEBuffer 3	New England Biolabs	Cat#B7003
Critical Commercial Assays		
RNAqueous Total RNA Isolation Kit	Thermo Fisher Scientific	Cat#AM1912
RiboPure RNA Purification Kit	Thermo Fisher Scientific	Cat#AM1924
Reverse Transcription System	Promega	Cat#A3500
Power SYBR Green PCR Master Mix	Thermo Fisher Scientific	Cat#4367659
DreamTaq Green PCR Master Mix	Thermo Fisher Scientific	Cat#K1081
Western Lightning Plus-ECL Substrate	Perkin Elmer	Cat#NEL103E001EA
Experimental Models: Cell Lines		
293FT human fibroblasts	Thermo Fisher Scientific	Cat#R70007
Experimental Models: Organisms/Strains		
Sprague Dawley rat	Taconic or Charles River	NTac:SD (RRID: RGD_1566440); Crl:SD (RRID: RGD_737891)
C57BL/6 mouse	Taconic or Charles River	C57BL/6NTac (RRID: IMSR_TAC:b6); C57BL/6NCrl (RRID: IMSR_CRL:27)
MYPT1 fl/fl conditional knockout mouse	Min-Sheng Zhu (Wenzhou Medical College) and James Stull (University of Texas Southwestern)	PMID: 23499953; RRID: MGI:5559689
Oligonucleotides		
See Tables S2 and S3	N/A	N/A
Recombinant DNA		
pLL3.7_shScramble	This paper	N/A
pLL3.7_shAnkG_rat	This paper	N/A
pLL3.7_shNaV1.x_rat	This paper	N/A
pLL3.7_shBIVspectrin_rat	This paper	N/A
pLL3.7_shMYPT2_mouse	This paper	N/A
Software and Algorithms		
Nikon NIS Elements Software	Nikon	N/A
ImageJ	NIH	N/A
MATLAB	MathWorks	N/A

CONTACT FOR REAGENT AND RESOURCE SHARING

Requests for reagents and additional information should be directed to the Lead Contact, James Salzer (james.salzer@nyumc.org).

EXPERIMENTAL MODEL AND SUBJECT DETAILS**Primary Neuron Cultures from E18 Rat Hippocampus and Cortex**

All rodent experiments were carried out under an approved animal protocol and in accordance with the guidelines of the Institutional Animal Care and Use Committee of the New York University School of Medicine. The protocol for primary rat hippocampal cultures has been previously published ([Dzhashiashvili et al., 2007](#)) with minor modifications. Pregnant Sprague-Dawley rats (Charles River or Taconic) were sacrificed via CO₂ asphyxiation and subsequent cervical dislocation. Embryos were pooled and dissected irrespective of sex. The E18 embryonic hippocampus or cortex was isolated and meninges removed in ice cold dissecting solution (PBS, 10 mM HEPES, 0.6% glucose). Tissue was dissociated in 0.25% trypsin, triturated, centrifuged, and resuspended in plating medium (MEM, 10% FBS, 2 mM L-glutamine, 1 mM sodium pyruvate, 0.45% glucose, penicillin/streptomycin). For most experiments, glass

coverslips (12mm diameter, No. 0, Karl Hecht) were coated overnight with 0.1 mg/mL poly-L-lysine prior to dissection. Cells were plated at a density of ~ 200 cells/mm² (35,000 cells/15mm dish) in plating medium. After 3 hr, medium was changed to culture medium (Neurobasal, B27 supplement, 0.5 mM L-glutamine, penicillin/streptomycin) supplemented with fluorodeoxyuridine. Neurons were maintained in a humidified incubator at 37°C and 5% CO₂. Fifty percent media changes were performed every third day, supplementing with fluorodeoxyuridine on DIV4 and DIV7. The day of plating was considered DIV0 for all studies; all experiments were performed at DIV10 unless otherwise noted.

Conditional MYPT1 Knockout Mice

MYPT1^{fl/fl} mice (He et al., 2013) were obtained from Min-Sheng Zhu (Wenzhou Medical College) and James Stull (UT Southwestern). After rederivation at the Rodent Genetic Engineering Core at NYU School of Medicine, homozygous fl/fl mice were maintained on the C57BL/6 background and were crossed for at least three generations prior to experiments. The Flox allele was genotyped using published primers GCAGTCCTCTTGCCCAAATG and GTGTGCTACCACCATGGAGC, with a 350 bp amplicon indicating the floxed allele and a 250 bp amplicon indicating the wild-type allele (Table S2). The absence of germline Cre was confirmed by PCR. Mice were maintained under standard husbandry conditions at an NYU vivarium under an approved animal protocol.

Primary Neuron Cultures from E18 Mouse Hippocampus and Cortex

Timed pregnant C57BL/6 mice were provided by commercial vendors (Charles River or Taconic). For MYPT1 conditional knockout studies, timed pregnancies of MYPT1^{fl/fl} mice were established at the NYU vivarium. Dissections were performed at E18 and were similar to wild-type rat cultures, with the following exceptions: tissue was dissociated in papain (Worthington) and quenched with trypsin inhibitor (Sigma) to improve neuronal survival. Viability assessed by trypan blue exclusion was routinely >95% at the time of neuronal plating. Neurons were plated on poly-L-lysine coated coverslips at ~ 550 cells/mm² (100,000 cells/15mm coverslip) and were subsequently maintained under identical conditions to rat neuronal cultures.

METHOD DETAILS

MYPT1 Knockout Experiments

MYPT1^{fl/fl} neurons were infected on DIV1 with either AAV1-CMV-HI-eGFP-Cre-WPRE-SV40 (“AAV1-Cre”) or AAV1-CMV-PI-eGFP-WPRE-bGH (“AAV1-EGFP”) as a control. Both infections were at an MOI of $\sim 1 \times 10^5$ from single-use frozen aliquots of virus stored at -80°C . Viruses were purchased from the Penn Vector Core. Infection efficiency was high and toxicity was limited based on EGFP labeling and visual inspection of cultured neurons, respectively. Neurons were examined at DIV12 or later.

Lentiviral Knockdown Experiments

Knockdowns of AnkG, NaV, and β IV spectrin were performed in wild-type rat cultures, while knockdown of MYPT2 was performed in wild-type mouse cultures to allow direct comparison with MYPT1^{fl/fl} knockout neurons. We designed and tested several AnkG and MYPT2 shRNA sequences following published protocols. Pan-NaV alpha subunit and β IV spectrin shRNA sequences were previously published (Hedstrom et al., 2007). Scrambled shRNA sequence was previously validated by our laboratory (Dzhashashvili et al., 2007; Zhang et al., 2012). For all targets, RNAi stem loop oligonucleotides (see Table S3 for sequences) were custom synthesized (IDT) and cloned into pLL3.7, a lentiviral plasmid for shRNA expression, at the HpaI and XhoI sites (Rubinson et al., 2003), following standard protocols. Lentivirus was produced by co-transfection of pLL3.7 and the second-generation packaging plasmids VSVG and Δ 8.9 into subconfluent 293FT cells. Viral supernatant was collected after 72 hr, centrifuged, filtered, aliquoted, and stored at -80°C . Neurons were infected at DIV1 by adding 50 λ viral supernatant directly into 200 λ Neurobasal/B27 per coverslip and were maintained until at least DIV12 to ensure complete knockdown. Robust infection efficiency was demonstrated by EGFP expression from an alternative promoter on pLL3.7, while knockdown efficiency of AIS targets was measured locally by immunofluorescence of the AIS on DIV12.

Pharmacology and Depolarization Experiments

For all pharmacology experiments, stock solutions were prepared, aliquoted, and stored per manufacturer’s recommendations. Aliquots were equilibrated to room temperature for at least 1 hr prior to use. Final working stocks were made in Neurobasal/B27 medium immediately prior to application to live cultures. A vehicle control (usually DMSO) was used in parallel; final DMSO concentrations never exceeded 0.3% (v/v). For depolarization experiments, KCl was dissolved in fresh Neurobasal/B27 medium. Experiments ≤ 1 hr duration were performed in 100% fresh Neurobasal/B27 medium. Experiments lasting longer than 1 hr, as well as those in which drugs were preincubated or washed out, were performed in 50% conditioned medium and 50% fresh medium to improve neuron survival. Cell viability in all manipulations was visually confirmed using both DIC microscopy of freshly fixed cells and with subsequent immunofluorescence of MAP2 and EGFP, where applicable.

Key reagents used in these experiments included: blebbistatin, ML7 hydrochloride, KN-93, Y27632, calyculin A, okadaic acid ammonium salt (used at 1 μM to inhibit PP1 and PP2A, and 2 nM to selectively inhibit PP2A), fostriecin sodium salt, cyclosporin

A, FK506, nimodipine and phalloidin oleate (all from Sigma); SNS-314 mesylate (from Selleck); jasplakinolide (from Santa Cruz); and tetrabromobenzotriazole (TBB), SC-514, KT-5720, and MDL28170 (all from Tocris). See also [Table S1](#) for details on myosin kinase inhibitor experiments.

Optogenetic Stimulation of Cultured Neurons

Cultured rat hippocampal neurons were infected with AAV1-CAG-ChR2-Venus (SignaGen) at an MOI of 10^5 on DIV3. ChR2 immunofluorescence was monitored by expression of the Venus tag, which was robust within 4-5 days post-infection. Infected neurons were stimulated on DIV10 using a 470 nm/17.2 mW fiber-coupled LED (Thor Labs) connected to a programmable LED driver (Thor Labs). The stimulation protocol was programmed via a Master-8 pulse stimulator (AMPI) following a published pattern for induction of short-term AIS remodeling ([Evans et al., 2015](#)). Briefly, coverslips were stimulated at 5 s intervals with a burst consisting of 5x5 ms flashes at 20 Hz; this pattern repeated for 15 min. Coverslips were stimulated in Neurobasal/B27 on a heat block at 37°C; control coverslips were maintained in parallel on the heat block, wrapped in foil. Coverslips were subsequently fixed and prepared for immunofluorescence and imaging as detailed below. Of note, micrographs depict native Venus fluorescence and were not amplified by anti-EGFP immunofluorescence. Stimulated neurons were grossly normal in morphology by Venus expression and MAP2 staining.

Immunofluorescence of Neuronal Cultures

Cultured neurons were fixed for 10 min with freshly prepared 2% PFA in PBS followed by three washes with PBS. For Triton extraction experiments, neurons were incubated in extraction solution (0.5% Triton X-100, 30 mM PIPES, 1 mM magnesium chloride, 0.5 mM EDTA in PBS) for 30 s then washed thoroughly prior to fixation with PFA. Neurons were blocked for 1 hr at room temperature in blocking solution (5% BSA, 1% donkey serum, 0.2% Triton X-100) prior to overnight incubation at 4°C with primary antibodies in 5% BSA, 0.2% Triton X-100. Secondary labeling with donkey Alexa Fluor antibodies (Invitrogen; 405, 488, 594, 680; 1:1,000 dilution) was carried out for 2 hr at room temperature. Coverslips were washed several times with PBS and then distilled water, mounted on glass slides in Fluoroshield (Sigma), and dried overnight prior to imaging.

Primary antibodies used were: rabbit pMLC Thr18/Ser19 (Cell Signaling); mouse monoclonal AnkG (Santa Cruz); and chicken MAP2 (Encor). Additional antibodies include: rabbit total myosin regulatory light chain (Cell Signaling); rabbit non-muscle MHCs A, B, and C (Covance); rabbit myosin essential light chain (Bioss); goat GFP (ABD Serotec); mouse monoclonal tau (BD); mouse monoclonal β IV spectrin, AnkG (in knockdown experiments), pan-neurofascin, and Kv2.1 (all from Neuromab); mouse monoclonal pan-NaV (Sigma); chicken MBP (Millipore); guinea pig Caspr (gift of Dr. M. Bhat); rabbit beta-IV spectrin (gift of Dr. M. Rasband).

Imaging of Cultured Neurons

Images of cultured neurons were taken on a Nikon Ti inverted microscope equipped with a Lambda LS xenon arc lamp (Sutter) and a DS-Qi2 CMOS camera (Nikon). Representative images were taken at 100x magnification as z series. For experiments showing protein localization in multiple neurons (e.g., myosin hexamer subunits) or in distal axons (e.g., MYPT1 and MYPT2 neurons), wide-field images were obtained at 63x magnification. Image stacks were computationally focused using the extended depth of field function in the Nikon NIS Elements software. Kv2.1 puncta were further resolved using the deconvolution function of the Nikon NIS Elements software. Images were minimally processed for brightness and contrast in Photoshop (Adobe). All panels within an experiment were imaged at the same session and processed using identical settings in Photoshop.

Imaging of Nerve and Mouse Brain Sections

Teased sciatic nerves from adult (~P30) wild-type mice and optic nerves from adult (~P60) wild-type mice were obtained as previously described ([Rios et al., 2000](#)), fixed with 1% PFA, and stained following the protocol for cultured neurons above. Myelinating cocultures consisting of rat dorsal root ganglion sensory neurons and Schwann cells were established following published protocols ([Dzhashiashvili et al., 2007](#); [Zhang et al., 2012](#)) and were allowed to myelinate for at least two weeks prior to fixation with 2% PFA and staining. Sciatic nerves and cocultures were imaged on the Nikon Ti microscope. Axial projections of sciatic nerve were obtained on a Zeiss LSM 880 confocal microscope equipped with Airyscan. Optic nerves were imaged on a Zeiss LSM 510 confocal microscope.

Mouse brains were obtained similar to published protocols ([Samanta et al., 2015](#)), with minor modifications. Briefly, adult wild-type C57BL/6 mice (~P30) were deeply anesthetized with pentobarbital and phenytoin (Beuthanasia, Merck) prior to transcardial perfusion with cold PBS and 1% PFA. Brains were removed and post-fixed for 2 hr in 1% PFA, equilibrated with 30% sucrose overnight, and embedded in OCT for sectioning. 20 μ m thick coronal sections were taken through the corpus callosum and hippocampus. In brain sections, AIS antigens were found to be sensitive to overfixation, with pMLC demonstrating significant sensitivity. Consequently, brains were fixed with 1% PFA and slides were treated with antigen retrieval prior to staining. Slides were heated in 30 mM sodium citrate, pH 6, for 20 min at 95°C, then cooled to room temperature in the citrate solution prior to blocking and immunofluorescence. To minimize background fluorescence in brain and optic nerve tissues, the previously described staining protocol for cultured cells was slightly modified as follows: Sections were blocked with 10% goat serum in tissue buffer (1% BSA, 0.25% Triton X-100). Alexa Fluor secondary antibodies raised in goat were used at a dilution of 1:5,000. Tissues were mounted in Fluoroshield and allowed to dry overnight prior to imaging on a Zeiss LSM 510 confocal microscope.

RNA Expression Experiments

mRNA was isolated from rat DIV10 hippocampal cultures (RNAqueous, Ambion) and from adult Sprague-Dawley rat tissues (RiboPure, Ambion) following manufacturer's protocols. For mRNA extraction, neurons were plated on 60 mm plastic dishes at an elevated density of ~ 530 cells/mm² (1.5×10^6 neurons/dish). First strand cDNA was generated using oligo-dT primers (Promega). MLC isoform expression was tested quantitatively using Power SYBRGreen master mix (Thermo) on a Stratagene Mx3005p qPCR thermal cycler (Agilent). Thermal cycling and data processing were performed following manufacturer's recommendations. The Ct values for each MLC amplicon were internally normalized to GAPDH in each sample; fold difference was subsequently calculated relative to Myl9 expression, which was low in all samples, to allow relative comparison of each isoform across tissues. MYPT isoform expression was evaluated qualitatively by standard PCR using DreamTaq master mix (Thermo) and agarose gel electrophoresis. For all experiments, primers were designed using online Primer3 and NCBI software and were validated for specificity by NCBI Blast (see [Table S2](#) for primer sequences).

Western Blots

DIV10 rat hippocampal neurons were treated as indicated then lysed with 2% SDS, 25 mM Tris pH 7.5, protease inhibitors (Roche), and phosphatase inhibitors (Roche). Equal amounts of protein were loaded onto a 15% SDS-PAGE gel and transferred to nitrocellulose. Membranes were blotted with rabbit pMLC (Cell Signaling), rabbit total MLC (Abcam), and mouse alpha tubulin (Sigma) and developed by ECL following manufacturer's protocols (Perkin-Elmer). Band intensities were measured in ImageJ and normalized to tubulin.

Phosphatase Treatment of Cultured Neurons

For immunofluorescence, DIV10 rat hippocampal neurons were fixed for 10 min in 1% PFA, washed thoroughly in PBS followed by 0.9% saline, then treated for 3 hr with phosphatase buffer \pm enzyme at 37°C. Calf intestinal phosphatase (CIP, New England Biolabs) was used at a concentration of 1 unit/ μ l in 1x NEB Buffer 3 (New England Biolabs). Lambda phosphatase was used at a concentration of 40 units/ μ l in 1x Protein MetalloPhosphatase Buffer with 1 mM MnCl₂ (New England Biolabs).

For western blots, neurons were lysed in 2% SDS/25 mM Tris as described above then passed three times through a Microcon YM-10 ultracentrifuge filter (Amicon) to remove SDS. Each centrifugation step was done at 12,000 rpm for 45-60 min at 4°C followed by reconstitution of the filtrate in 10x volume of fresh 25 mM Tris. Washed lysate was treated with phosphatase buffer \pm enzyme for 1 hr in a 40 μ L reaction. For CIP, 25 μ g lysate was incubated with 30 units of enzyme in NEB Buffer 3 at 37°C. For lambda phosphatase, 25 μ g lysate was incubated with 400 units of enzyme in PMP buffer with 1 mM MnCl₂ at 30°C. Samples were subsequently loaded onto SDS-PAGE gels and blotted as described above.

2D STORM Imaging

Preparation and Staining of Neuron Cultures

Rat hippocampal neuron cultures were plated on 18 mm circular coverslips in 35 mm plastic dishes at a slightly elevated density (~ 520 cells/mm², 500,000 neurons/35mm well). Cultures were otherwise established and maintained as previously described. DIV10 neurons were treated with either 50 mM KCl depolarization or 5 mM KCl control Neurobasal/B27 medium for 15 min prior to fixation. A fixation protocol for the detection of AIS proteins by STORM has been previously described ([Zhong et al., 2014](#)). Briefly, cultures were fixed for 1 min in 0.3% glutaraldehyde and 0.25% Triton X-100; fixed for an additional 15 min in 2% glutaraldehyde; and subsequently treated for 7 min with 0.1% sodium borohydride. The first two fixation steps were performed in a buffer consisting of 10 mM MES, 150 mM NaCl, 5 mM EGTA, 5 mM glucose, and 5 mM MgCl₂. Samples were blocked in PBS containing 2% glycine, 2% BSA, 0.2% gelatin, and 50 mM NH₄Cl for 30 min. Primary antibody against pMLC Thr18/Ser19 (rabbit, Cell Signaling) was diluted 1:200 in blocking solution and incubated overnight at 4°C. Primary antibody was then washed with PBS. The secondary antibody rabbit Alexa Fluor 647 (1:3,000, Life Technologies) and conjugated phalloidin-Atto488 (1:40, Sigma) to label actin were incubated for 1 hr at room temperature. Neurons were stored in PBS with phalloidin-Atto488 at 1:40 to maximize actin signal prior to imaging.

STORM Imaging and Image Analysis

STORM imaging was performed on an N-STORM microscope (Nikon) as previously described ([Leterrier et al., 2015](#)). After locating a suitable neuron using low-intensity illumination, an epifluorescence image was acquired followed by STORM acquisition. Alexa 647-conjugated pMLC was imaged first in STORM buffer (Abbelight) using 647 nm laser excitation, recording 50,000 frames at 67 Hz. Medium was then exchanged with a phosphate buffer (pH 7.4, 0.1 M) for imaging the Atto 488-conjugated phalloidin using 488 nm laser excitation, recording 50,000 frames at 67 Hz. N-STORM software (Nikon) was used for localization of single fluorophore activations and the correction of chromatic aberration and shift between channels. The list of localizations was then exported as a text file. Image reconstructions were performed using the ThunderSTORM ImageJ plugin ([Ovesný et al., 2014](#)) in Fiji software. Custom scripts and macros were used to translate localization files from N-STORM to ThunderSTORM formats, as well as to automate image reconstruction for whole images, detailed zooms, and YZ transverse projections ([Leterrier et al., 2015](#)). Actin images were equally adjusted with a global 0.7 gamma factor to aid visualization of faint structures.

QUANTIFICATION AND STATISTICAL ANALYSIS

Quantitative AIS Image Analysis

Imaging

All experiments were carried out in ≥ 3 independent replicates; one representative experiment was selected for quantification and analysis. Investigators were blinded to the experimental conditions being imaged and quantified. Images were captured with a Nikon Ti inverted microscope using a 63x objective and taking z series which were subsequently focused in the Nikon NIS Elements software. Fields were selected on the basis of MAP2-positive somata only, allowing a random sampling of neurons on each coverslip irrespective of experimental condition. For a typical experiment, 30-40 random fields were captured across three coverslips to sample 50-70 AIS or axons per condition; this n was empirically determined to capture the variability of an average culture, as further increases to n did not substantially change averages or SEMs. To ensure reproducibility of intensity measurements, all images within an experiment were captured in one microscopy session using consistent microscope and software settings.

AIS and Axon Tracing

Computationally focused images were analyzed in the Nikon NIS Elements software using the intensity profile function. Each AIS was manually traced by drawing a 6 pixel wide ($\sim 0.75 \mu\text{m}$) line down its center. A linear intensity profile was generated for all 3-4 fluorescent channels by averaging this 6 pixel wide trace to one dimension. For most experiments, the beginning of the AIS was defined visually as the point where one or more fluorescent markers appeared to rise above background intensity. For developmental time course experiments, the axon was alternatively traced from its origin at the soma, irrespective of AIS start site. Intensity profiles were exported to Microsoft Excel and processed using a custom-written MATLAB script (available upon request). Background intensity from an acellular region of each image was subtracted from all pixels of that image during analysis.

To minimize biological assumptions about AIS start and end points, analysis was performed in one of two contiguous spatial windows: 0-60 μm from the origin, representing the AIS, or 61-120 μm from the origin, representing a proximal portion of the axon distal to the AIS. The first window captured the entirety of every AIS at all ages, while the second window generally displayed low fluorescence of AIS markers only slightly above background in mature control neurons. Due to the increased variability of cultured mouse neurons in comparison with rat neurons, AIS intensity was obtained as above while the distal axon intensity was obtained by random sampling of at least $n = 50$ segments on the coverslip, each of which was 60 μm in length and was not adjacent to an identifiable soma or AIS.

Data Analysis

For total intensity analysis, presented as bar graphs throughout, all background-subtracted pixels within each 60 μm window were summed, providing an equivalent to area under the curve for each AIS or axon. Data are presented as average intensities \pm SEM of all traces in each condition. For spatial intensity profiles, the axons were aligned at the first pixel and averaged across all traces per condition. These profiles were qualitatively similar across many sampled experiments, demonstrating the reliability of the alignment strategy. Data are plotted as average \pm SEM for each pixel and may be minimally smoothed in a 5 pixel ($\sim 0.6 \mu\text{m}$) frame.

Statistical Analysis and Graphing of Data

The AIS intensities measured were consistently non-normally distributed; they typically included a lengthy right tail comprising the distal AIS. Consequently, significance calculations for these experiments utilize the non-parametric Mann-Whitney test (for $n = 1$ comparisons) or Kruskal-Wallis test with Dunn's correction for multiple comparisons (for $n > 1$ comparisons). Statistical significance calculations were performed for each antibody/antigen independently. qPCR data were analyzed using two-way ANOVA with Tukey's correction for multiple comparison. Statistical comparisons in the STORM dataset used unpaired two-tailed t tests. All statistical calculations were performed in GraphPad Prism using standard settings; graphs were generated in Microsoft Excel. We use standard notation for p values in figures and legends: ns, $p > 0.05$; * $p \leq 0.05$; ** $p \leq 0.01$; *** $p \leq 0.001$; **** $p < 0.0001$.

DATA AND SOFTWARE AVAILABILITY

The custom-written MATLAB script for processing of AIS intensity files is available upon request.